

Block kinematics of the Pacific–North America plate boundary in the southwestern United States from inversion of GPS, seismological, and geologic data

Robert McCaffrey

Department of Earth and Environmental Sciences, Rensselaer Polytechnic Institute, Troy, New York, USA

Received 8 July 2004; revised 20 February 2005; accepted 15 March 2005; published 6 July 2005.

[1] The active deformation of the southwestern United States (30° – 41° N) is represented by a finite number of rotating, elastic-plastic spherical caps. GPS-derived horizontal velocities, geologic fault slip rates, transform fault azimuths, and earthquake-derived fault slip vector azimuths are inverted for block angular velocities, creep on block-bounding faults, permanent strain rates within the blocks, and the rotations of 11 published GPS velocity fields into a common North American reference frame. GPS velocities are considered to be a combination of rigid block rotations, recoverable elastic strain rates resulting from friction on block-bounding faults, and nonrecoverable strain rates resulting from slip on faults within the blocks. The resulting Pacific–North America angular velocity is similar to some published estimates and satisfies transform azimuths and one spreading rate in the Gulf of California, earthquake slip vectors in the Gulf of California and Alaska, and GPS velocities along coastal California and within the Pacific Basin. Published fault slip rates are satisfied except in the southern Mojave Desert where the motion of the Mohave block relative to North America is faster than can be explained by mapped faults. The largest blocks, the Sierra Nevada–Great Valley and the eastern Basin and Range, show permanent strain rates, after removing elastic strain, of only a few nanostrain per year, demonstrating approximately rigid behavior. Observed horizontal strain rates correlate strongly with predicted strain rates from known faults suggesting that the short-term strains evident in GPS velocities are largely elastic. In only about 20% of the region is distributed deformation needed to match the data, indicating that a plate tectonic style description of the deformation of the western United States is plausible. Most blocks rotate about vertical axes at approximately the same rate as the Pacific (relative to North America), suggesting that locally, spin rates are communicated from block to block, arguing against both floating block and ball-bearing mechanisms of block rotation. The similarities of the blocks' spin rates to that of the Pacific suggests that the Pacific strongly influences their motions through edge tractions. However, it is shown that the blocks cannot rotate about the Pacific–North America pole without spinning counter to the sense of Pacific–North America shear. Unlike some other broad plate boundaries, in the western United States, vertical axis rotations take up very little of the slip rate budget across the region.

Citation: McCaffrey, R. (2005), Block kinematics of the Pacific–North America plate boundary in the southwestern United States from inversion of GPS, seismological, and geologic data, *J. Geophys. Res.*, *110*, B07401, doi:10.1029/2004JB003307.

1. Introduction

[2] Whether continental deformation is best represented by a series of rotating, rigid spherical caps in the manner of plate tectonics [King *et al.*, 1994; Thatcher, 1995; Tapponnier *et al.*, 2001], by elastic-plastic blocks [Peltzer and Tapponnier, 1988], by blocks separated by discrete, deforming zones [Thatcher, 2003], or by a more spatially continuous process such as flow of a viscous substrate

[England and McKenzie, 1982; Molnar, 1988; Jones *et al.*, 1996; Bourne *et al.*, 1998; Flesch *et al.*, 2000] remains largely unresolved. Difficulties arise because the long-term surface deformation is clearly localized along faults yet the importance of the faults in the overall mechanical behavior of the lithosphere is unknown. In the continuum concept, the forces that drive the surface blocks are derived by basal shear and faults offer little resistance whereas in the micro-plate model the forces more likely act along the edges of the plates; that is, they act across the lithosphere-scale faults. Continuum models have successfully reproduced certain aspects of the deformation field of the western United States

and other continental regions but such success in fitting observations neither proves the concept nor precludes other possibilities. Here I show that the active deformation of the western United States can be explained by a finite number of rotating, elastic spherical blocks with a relatively minor amount of small-scale deformation. In this case, most of the decade-scale surface strain rates observed in GPS velocities may be elastic and the long-term strains are localized along a few widely spaced faults.

2. Data and Analysis

[3] The wide Pacific–North American plate boundary in the southwestern United States is represented as a series of rotating plates, called blocks, of various sizes separated by faults (Figure 1). The description of the motions of the blocks is mathematically identical to methods of estimating rotations of the large tectonic plates on the Earth's surface [Morgan, 1968; Minster *et al.*, 1974; DeMets *et al.*, 1990]. A complexity in applying plate tectonic concepts directly to small regions, particularly when using short-term geodetic data, is that, in addition to rotations, increases in stress through time on the block-bounding faults result in elastic strain rates within the blocks. The strain rates cause surface velocities derived from Global Positioning System (GPS) measurements, which now comprise most of the available kinematic data, to deviate from those expected from rotations alone and therefore do not comply with the “rigid plate” requirements of plate tectonics. Here, using the “back-slip” approach of Savage [1983] and the elastic half-space formulas of Okada [1985], the strain rates arising from such fault stress changes are estimated simultaneously with the block motions [McCaffrey *et al.*, 2000].

[4] In addition to solving for block rotations and fault characteristics, here I use two additional types of parameters in the inversion: one to represent nonrecoverable, horizontal strain rates within the blocks and another to rotate published GPS-derived velocity fields into a common reference frame. The short-term strain rate within a block can comprise a recoverable (elastic) part due to stress changes on its bounding faults and a nonrecoverable (permanent) part that likely occurs by slip or localized strain on internal faults. In the long run, the elastic strain does not result in changes to the block's shape whereas the permanent strain does; such behavior is often, but not uniquely, represented by an elastic-plastic rheology [e.g., Turcotte and Schubert, 1982; Peltzer and Tapponnier, 1988]. In this paper, the inclusion of permanent strain rates within blocks is intended to represent more distributed deformation on faults at scales smaller than can be reasonably represented by blocks. The horizontal strain rate tensor for a spherical Earth is given by Savage *et al.* [2001]; the east and north velocities are

$$V_\varphi(\varphi, \theta) = e_{\varphi\varphi} R_e \sin \theta_0 (\varphi - \varphi_0) + e_{\varphi\theta} R_e (\theta - \theta_0)$$

$$V_\theta(\varphi, \theta) = e_{\varphi\theta} R_e \sin \theta_0 (\varphi - \varphi_0) + e_{\theta\theta} R_e (\theta - \theta_0),$$

where φ is longitude, θ is colatitude, R_e is the radius of the Earth, e_{ij} is the strain rate tensor, and (φ_0, θ_0) is the centroid of the block. When applied, the three independent components of the symmetric strain rate tensor, $e_{\varphi\varphi}$, $e_{\theta\theta}$, and $e_{\varphi\theta}$, are formally estimated in the inversion.

[5] The GPS-derived velocities used in this study are from 11 separate papers (Table 1); all in different reference frames. Three additional free parameters are included to rotate each of the velocity solutions into a common North American (NOAM) reference frame. The rotations of the velocity fields are done as part of the inversion, instead of prior to it, to take advantage of the strong spatial correlation among surface velocities inherent in the block model. This approach does not require that the velocity fields have common sites but does require that individual velocity fields span more than a single rotating block, though not necessarily the reference frame block.

[6] Angular velocities, creep distributions on faults, internal block strain rates, and GPS velocity field rotations are estimated by least squares fit to GPS vectors, fault slip rates, transform fault azimuths, and earthquake slip vectors [McCaffrey, 2002; R. McCaffrey, DEFNODE users' guide, <http://www.rpi.edu/~mccaffr/defnode/>]. The data comprise 1710 horizontal GPS velocities (from 1333 unique monuments) that fall within the model domain (Figure 2 and Table 2), 111 fault slip rates [Working Group on Northern California Earthquake Potential, 1996; Frankel *et al.*, 2002; Petersen and Wesnousky, 1994; California Geological Survey, Probabilistic Seismic Hazard Assessment Maps (PSHA), <http://www.consrv.ca.gov/CGS/rghm/psha/index.htm>] including one Gulf of California (GC) spreading rate [DeMets, 1995], five GC transform fault azimuths [DeMets *et al.*, 1990], and 127 earthquake slip vectors from the western United States, the GC, and Alaska [DeMets *et al.*, 1990; Deng and Sykes, 1997; Dziewonski *et al.*, 1981; Ekström *et al.*, 2005]. All data, their uncertainties, estimated values, and additional references are given in the auxiliary material.¹

2.1. Data Uncertainties

[7] Inferences drawn from the results, measures of how well the data are fit, and parameter uncertainties all depend on the assigned data uncertainties. The published GPS velocity fields use a variety of approaches to estimating uncertainties. In fact, the uncertainties assigned to velocities at some sites vary by an order of magnitude between published velocity solutions. Using the published uncertainties, four velocity fields that have been fit previously with kinematic models [Beavan *et al.*, 2002; McCluskey *et al.*, 2001; Murray and Segal, 2001; Z.-K. Shen *et al.*, The SCEC Crustal Motion Map, version 3.0, <http://epicenter.usc.edu/cmm3/>, hereinafter referred to as SCEC Crustal Motion Map (CMM3)] have resulting normalized RMS (NRMS) from my inversions ranging from 1.11 to 1.31 (Table 1). This level of fit suggests that the reported uncertainties are properly scaled, assuming the model is valid, in agreement with the original works. Measures of the goodness of fit used here are the normalized RMS,

$$\text{NRMS} = \left[N^{-1} \left(\sum_{i=1}^N r_i^2 / \sigma_i^2 \right) \right]^{1/2}$$

¹Auxiliary material is available at <ftp://ftp.agu.org/append/jb/2004JB003307>.

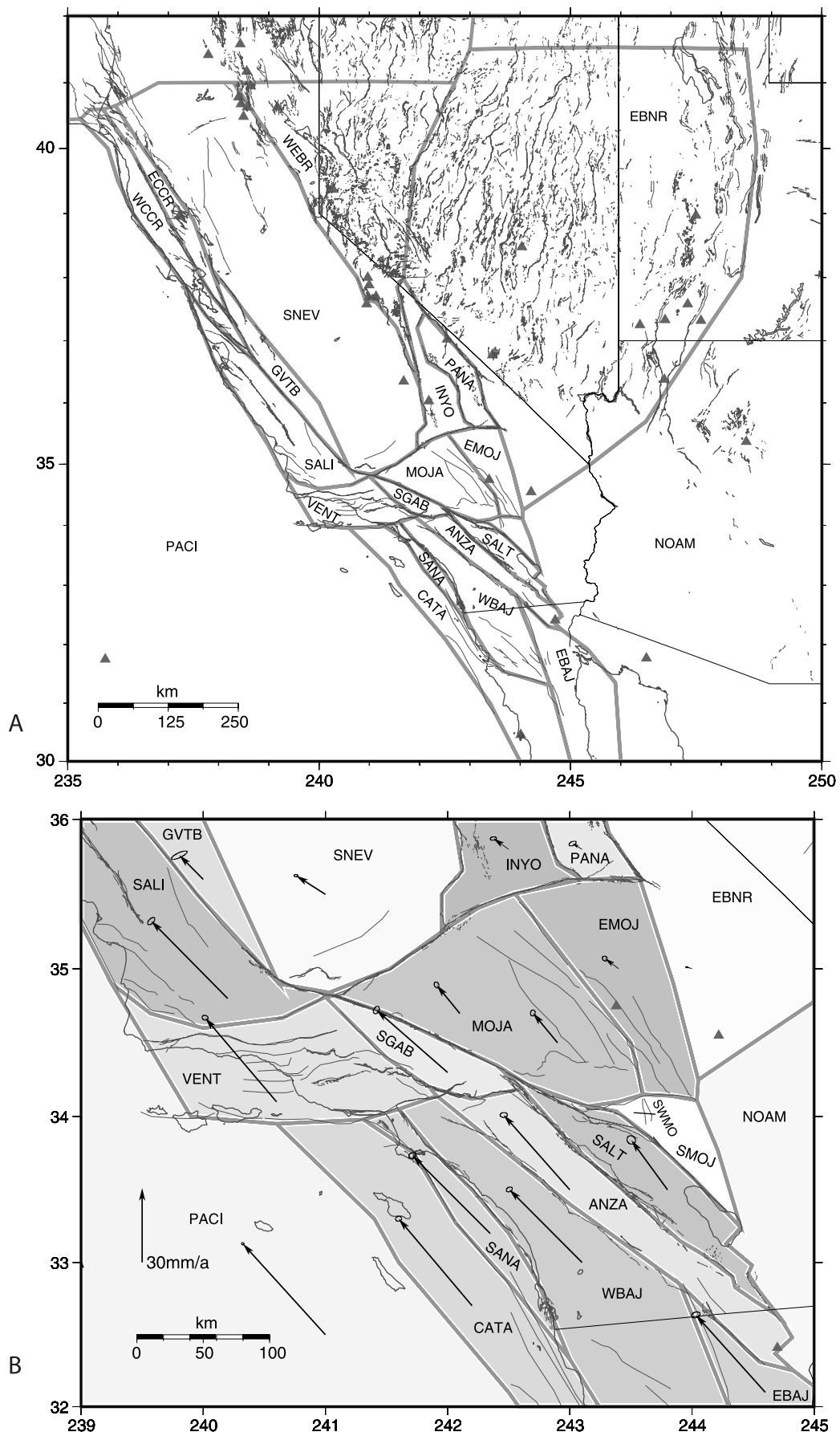


Figure 1

Table 1. Fits to Velocity Fields and the Poles of Rotation^a

Data	Factor	<i>N</i>	NRMS	WRMS	SumWt	RF	Longitude	Latitude	Omega	Sig Omega	Maxi	Min	Azimuth	Reference
ITRF	1.0	204	1.17	1.0	280	ITRF	277.09	-4.00	0.198	0.002	0.8	0.4	100.0	Boucher et al. [2004]
BEAV	1.0	46	1.31	0.7	159	ITRF	275.43	-5.97	0.194	0.002	1.0	0.5	91.9	Beavan et al [2002]
WUSC	2.5	492	1.01	1.1	430	NA	285.44	84.63	0.008	0.002	23.9	8.6	56.4	Bennett et al. [1999]
DXSN	1.0	30	1.22	1.2	32	NA	238.24	42.98	0.058	0.065	9.6	3.3	113.3	Dixon et al. [2000]
CMM3	1.0	1572	1.11	1.2	1393	NA	49.17	49.75	0.003	0.001	62.9	21.2	107.2	SCEC Crustal Motion Map
BARD	1.0	68	1.26	1.0	112	NA	59.00	-25.96	0.101	0.037	7.0	1.3	92.7	Murray and Segall [2001]
JF99	1.0	82	0.88	2.4	11	Pacific	30.13	-21.53	0.906	0.188	9.3	0.5	137.1	Freymueller et al. [1999]
MC01	1.0	166	1.12	0.6	527	NA	249.03	46.34	0.100	0.052	8.4	0.9	62.3	McCluskey et al. [2001]
DXB2	1.0	32	0.92	1.2	20	NA	246.82	31.52	0.082	0.267	11.8	4.3	175.3	Dixon et al. [2002]
TH01	1.0	130	1.26	1.2	143	NA	242.89	39.68	0.064	0.026	2.1	1.7	88.3	Thatcher et al. [1999]
RB03	2.5	224	1.24	0.8	587	NA	277.07	45.76	0.008	0.003	9.1	7.1	16.0	Bennett et al. [2003]

^aFactor is the scaling applied to the standard deviations of the velocities, *N* is the number of data, twice the number of vectors for GPS data, NRMS is the normalized RMS of the misfit, WRMS is the weighted RMS of misfits, SumWt is the sum of the weights for the velocities, RF is the original reference frame for the velocity field, Latitude, Longitude, and Omega give the Euler pole that rotates the velocity field into the North American reference frame, Sig Omega is the uncertainty in the rotation rate (degrees Ma), Max, Min, and Azimuth (degrees) are the 68% confidence error ellipse for the rotation of the velocity field, and Reference gives the source of the data.

and the weighted RMS,

$$\text{WRMS} = \left[\left(\sum_{i=1}^N r_i^2 / \sigma_i^2 \right) / \left(\sum_{i=1}^N 1 / \sigma_i^2 \right) \right]^{1/2},$$

where *r* is the residual, σ is the datum standard error, and *N* is the number of observations. The NRMS is a unitless indicator of how well the data are fit and should be near unity while the WRMS gives a measure of the a posteriori weighted scatter in the fits and has units of the measurement type.

[8] The largest GPS data set, the Southern California Earthquake Center CMM3 velocity field, which comprises 786 velocities, is fit with normalized RMS = 1.11 and weighted RMS = 1.2 mm/yr, indicating that the block model is capable of fitting the data at the published uncertainty level. In all but 2 of the velocity fields, I adopt the original uncertainties. For the WUSC [Bennett et al., 1999] and RB03 [Bennett et al., 2003] velocity fields, uncertainty scaling factors of 2.5 are applied. This value is based on statistical comparisons of the two velocity fields to each other and to CMM3 (Appendix A) and is within the range of uncertainty scaling factors of 2–3 suggested by Bennett et al. [2003] to be applied to their published uncertainties.

[9] Earthquake slip vectors derived from the Harvard centroid moment tensor solutions [Dziewonski et al., 1981] are assigned uncertainties of 10°, while earlier earthquakes from Deng and Sykes [1997] are assigned uncertainties of 20°. The focal mechanisms listed by Deng and Sykes [1997] as inferred from other nearby earthquakes (IOE) are not used. Slip vectors, transform azimuths, and spreading rates from DeMets [1995] and DeMets et al. [1990] are assigned the uncertainties from those papers. Fault slip rates from geologic studies are assigned uncertainties based on the range of their minimum and maximum values (see section 2.3).

2.2. Data Selection and Rejection

[10] Of the 1710 GPS vectors from the 11 velocity fields that fall within the model domain, 187 (11%) are rejected on the following basis: (1) Velocities that are visually different from nearby velocities (except when the site is near a fault). (2) Velocities in the WUSC solution that are updated in the RB03 solution but are more than 1.0 mm/yr different; and those from WUSC updated in the CMM3 solution that are more than 3.0 mm/yr different. (3) Sites near unmodeled faults such as the Cascadia, Aleutian, and Kamchatka subduction zones. (4) Sites near volcanoes. (5) Vectors with uncertainties larger than 8 mm/yr. Most (110) of the rejected velocities in categories (1) and (2) are redundant in that multiple velocity fields include the same sites. Rejected GPS velocities are fairly evenly distributed throughout the region and surrounded by well-fit sites (Figure 2a). Fits to selected and rejected GPS velocities are included in the online auxiliary material.

[11] Slip vector azimuths are taken from earthquakes that can be reasonably assigned to a fault (block boundary) and whose fault plane is consistent with the orientation of that boundary (Figures 2b, 3a, and 3b). Hence numerous earthquakes from the region are not used (but are shown in Figures 3a and 3b). Of the slip rate estimates for faults, again only those on block-bounding faults are used. In some cases, fault slip rate estimates at nearby localities differ significantly; all are kept to avoid bias to a particular set of parameters. The slip rates and slip vectors (and estimated values) from California and nearby are shown in Figures 3a, 3b, and 4. A complete listing is given in the auxiliary material.

2.3. Fitting Criteria

[12] The best fit parameters are those that minimize the reduced χ^2 statistic

$$\chi_n^2 = \left[n^{-1} \sum p_i \right]^{1/2},$$

Figure 1. (a and b) Block representation of the western United States. Each block is outlined by thick gray line and is bounded on all sides by faults (except at the northern edge of the region shown). Each block is assigned a four-letter code as used in the text and Table 3. Triangles are locations of volcanoes. Vectors in Figure 1b show calculated velocities relative to North America. Thin lines represent mapped faults.

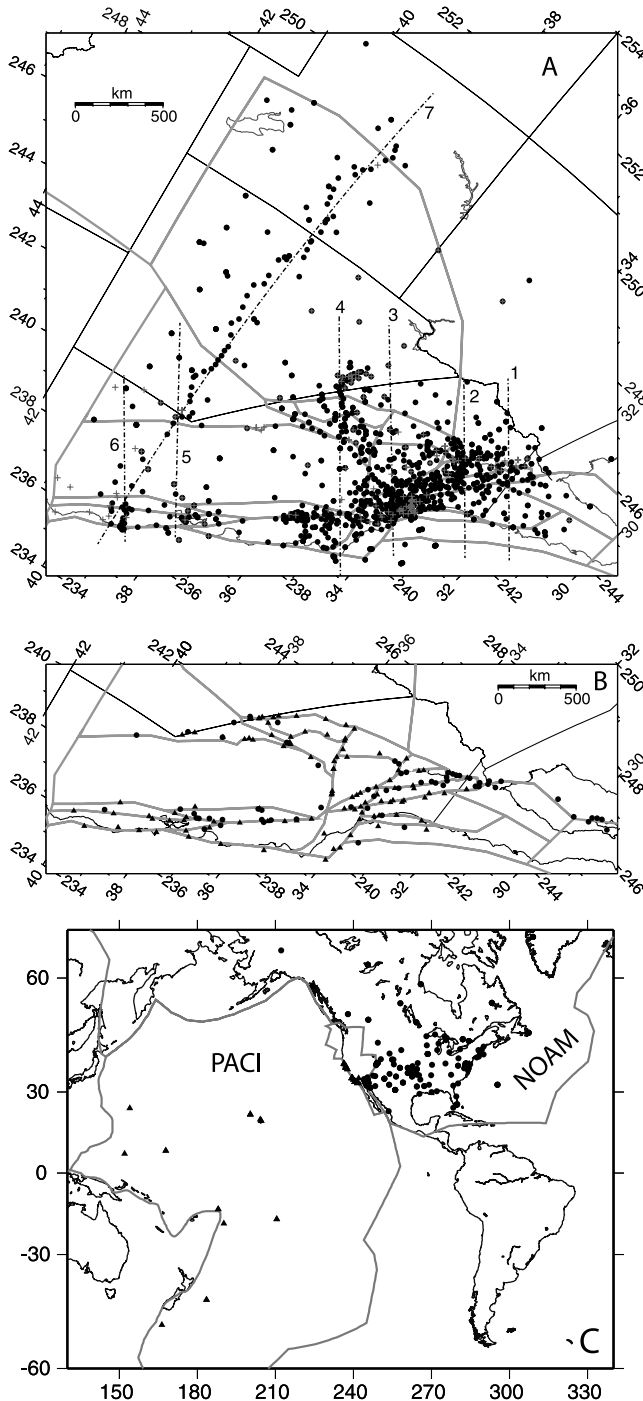


Figure 2. (a) Oblique projection of the western United States showing GPS sites used (dots) and those rejected (crosses). Assumed block boundaries are thicker gray lines. Dashed lines are locations of profiles shown in Figure 9 and are labeled by a profile number. (b) Locations of fault slip rates (triangles) and earthquake slip vector azimuths (dots) used in the inversion. (c) Locations of GPS velocities on the Pacific (triangles) and North American (dots) plates.

where n is the number of degrees of freedom (number of observations minus the number of free parameters), p is a data misfit penalty function, and the sum is over the number of observations. The penalty function depends on the data

type (see Appendix B). Additional penalties are applied to keep some free parameters within specified ranges, for example the creep fraction on the fault must stay between 0 and 1.

[13] Because the problem is nonlinear and hard parameter constraints are used, the minimum in χ^2_n is found by the method of simulated annealing [Press *et al.*, 1989]. Formal uncertainties are estimated at the best fit parameters by assuming linearity and using the a priori data uncertainties. F tests are used to infer whether the fits to the data resulting from changing the allowed parameters warrant that change. The F test assesses the change in weighted misfit variance (χ^2) resulting from a change in the number of degrees of freedom; the result of the F test is given as a probability that the misfit variance of a test run could be produced by a random sampling of the misfit variance of a control run.

2.4. Block Model

[14] Blocks (plates) are closed, spherical polygons on the Earth's surface and cover the entire model domain (Figures 1 and 2c). Each point within a block is assumed to rotate with the same angular velocity. In most of the study area, the block boundaries coincide with major faults while in other areas the choice is less clear. (Coordinates of block boundaries and faults are given in the auxiliary material.) The fault maps of Jennings [1974], Dixon *et al.* [2002], and the Southern California Earthquake Center Community Fault Model (A. Plesch, personal communication, 2003) are used as guides for block boundaries. The boundary between the deforming western Basin and Range (WEBR) and the eastern Basin and Range (EBNR, Figure 1a) is based largely on the GPS velocities [Thatcher *et al.*, 1999]. The Mojave region is separated into two blocks along the Calico-Blackwater fault (Figure 3b) which appears to be slipping relatively fast [Peltzer *et al.*, 2001] and several inversions are used to investigate possible block geometries in the Mojave region. Another unclear area is the southern end of the Great Valley thrust belt (GVT, Figure 3a); although it must extend south of the epicenter of the 1983 Coalinga earthquake (36°N, Figure 3a), how it connects with the San Andreas to the south of there is not obvious. At the far edges of the model domain the block boundaries are treated as fully creeping faults and therefore do not impact the model.

[15] Some regions, such as the Transverse Ranges (VENT), Mojave (MOJA and EMOJ), Basin and Range (WEBR and EBNR), and others, are included as blocks yet have mapped faults distributed throughout their interiors (Figure 1). In these cases, the block boundaries are drawn to encompass the regions of possible distributed permanent strain which is then represented in the model.

2.5. Faults

[16] Faults are represented by a series of node points within a spherical Earth that specify their 3-D shapes [McCaffrey, 2002; R. McCaffrey, DEFNODE users' guide, <http://www.rpi.edu/~mccaff/defnode/>] so that fault dip and curvature are approximated. Most faults are near vertical while some dip at lower angles when such information is available. All faults extend down to 20 km depth, below which they creep at the full relative plate velocity. End-to-end fault intersections are handled by smoothly varying fault orientations from either side of the intersection. Triple

Table 2. Summary of Fits to Data Types

Data Type	N^a	NRMS	WRMS
GPS velocities	3046	1.12	1.0 mm/yr
Slip rates	110	0.86	1.3 mm/yr
Slip azimuths	132	0.77	9.6°

^a N is the number of data, twice the number of vectors for GPS data.

junctions, where two faults meet at a T, are handled by a 3-D projection of the end of the truncated fault (stem of the T) onto the through going fault (top of the T). In this way, all faults end either at another fault, without gaps or overlaps, or outside the region of interest. Fault geometries in the structural model are fixed.

[17] Between fault nodes, the fault surface is approximated by tiling, using quadrilateral patches with dimensions of 2 km along strike and 1 km along the dip direction. The patches are not rectangles, as used by the *Okada* [1985] formulation, but are small enough that their deviations from rectangles do not matter; that is, in the limit as the patch

approaches a point source the shape does not matter, only the centroid, orientation, and area of the fault patch are important. Since the *Okada* [1985] routine uses Cartesian coordinates, the transformation from spherical coordinates is done locally with the fault segments at the origin to minimize distortion.

[18] Because of friction on the fault surface, the short-term slip rate (creep rate) across most faults is much less than the long-term slip rate expected from the relative motion of the adjacent blocks. The tendency for faults to be stuck for long periods of time is often referred to as “locking” or “coupling” and gives rise to elastic strain rates in the rocks adjacent to the fault. In light of confusion regarding what these terms mean [*Wang and Dixon*, 2004; *Lay and Schwartz*, 2004], to model the influence of faults on the velocities, I use a purely kinematic scalar quantity represented with ϕ . If V is the long-term slip vector on the fault (over many earthquake cycles) and V_c the short-term creep vector (the steady displacement rate across the fault surface over a short

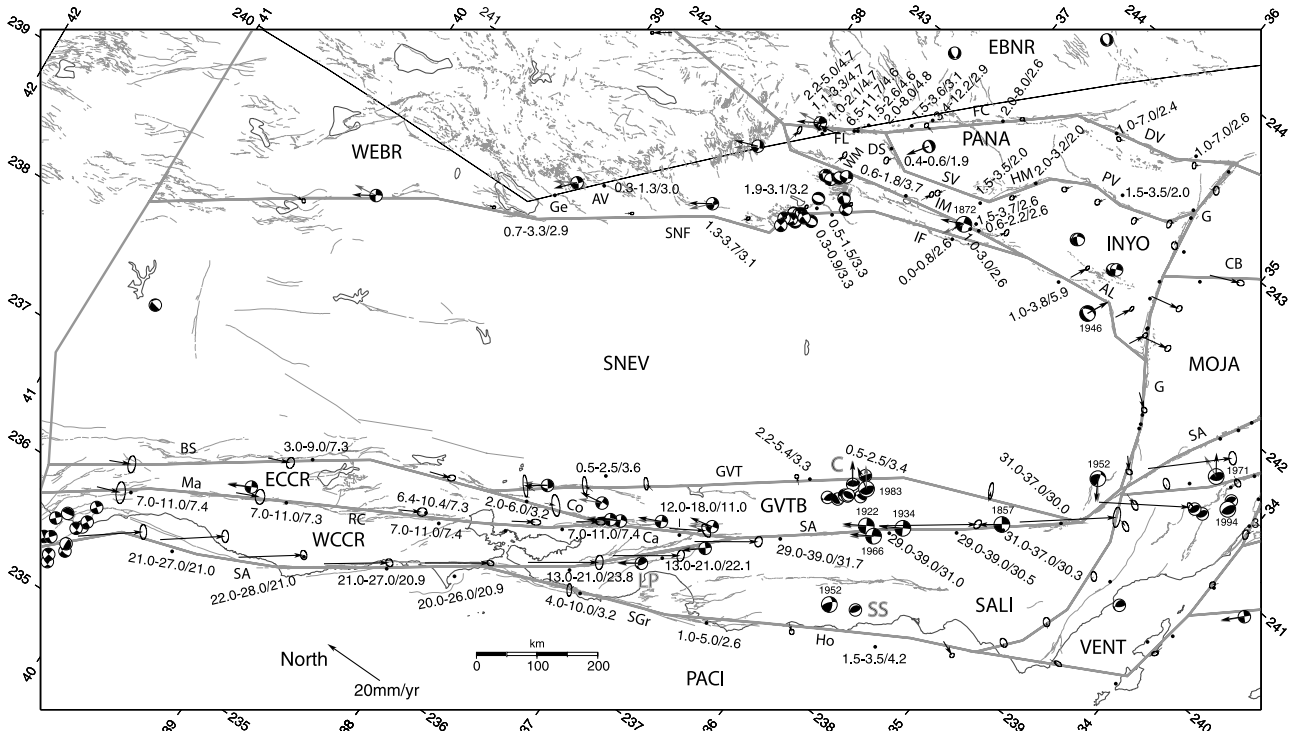


Figure 3a. Oblique projection about Pacific–North America pole of rotation showing mapped faults (thin lines), block boundaries (thicker gray lines), earthquake focal mechanisms, and fits to fault slip rate and slip vector data. Black vector at center of beach ball shows the observed slip vector azimuth; gray vectors are calculated azimuths. Black dots show locations of fault slip rate estimates; numbers near each give the minimum, maximum, and calculated values in the form minimum-maximum/calculated. Vectors along faults show the calculated fault slip vectors; the vector shows how the block containing the tail of the vector moves relative to the adjacent block. Small beach balls are from the Harvard CMT catalog, and the larger ones (labeled with year of occurrence) are from the compilation of large earthquakes by *Deng and Sykes* [1997]. Four-character block abbreviations are explained in Table 3. Fault abbreviations are as follows: AL, Airport Lake; AV, Antelope Valley; BS, Bartlett Springs; Ca, Calaveras; Co, Concord; DS, Deep Springs; DV, Death Valley; FC, Furnace Creek; FL, Fish Lake; G, Garlock; Ge, Genoa; GVT, Great Valley thrust; HM, Hunter Mountain; Ho, Hosgri; IF, Independence; IM, Inyo Mountains; Ma, Ma’acama; PV, Panamint Valley; RC, Roger’s Creek; SA, San Andreas; SGr, San Gregorio; SNF, Sierra Nevada frontal; SV, Saline Valley; WM, White Mountain. Large gray letters show recent earthquakes: LP, Loma Prieta; SS, San Simeon; C, Coalinga.

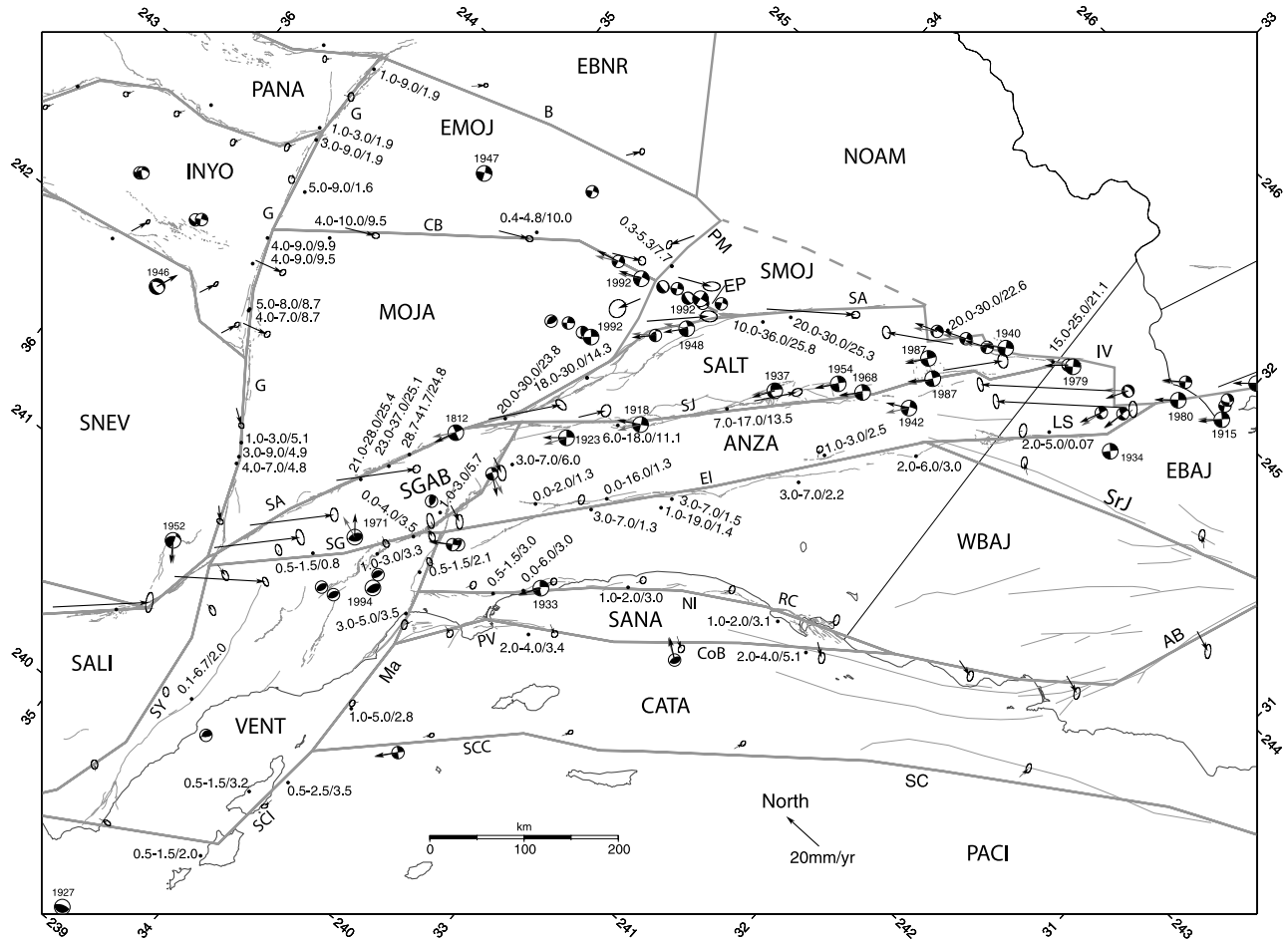


Figure 3b. As in Figure 3a. Fault abbreviations are as follows: AB, Agua Blanca; B, Baker; CB, Calico Blackwater; CoB, Coronado Bank; El, Elsinore; EP, Eureka Peak; G, Garlock; IV, Imperial Valley; LS, Laguna Salada; Ma, Malibu; NI, Newport Inglewood; PV, Palos Verdes; RC, Rose Canyon; SA, San Andreas; SCC, Santa Cruz/Catalina/San Clemente; SCI, Santa Cruz Islands; SG, San Gabriel; SJ, San Jacinto; SrJ, Sierra Juarez; SY, Santa Ynez.

time, presumably parallel to V , then $\phi = 1 - V_c/V$. If $\phi = 0$, creep occurs at the long-term fault slip rate and if $\phi = 1$, there is no creep on the fault in the interseismic period. In the following, I use the terms “stuck” for

$\phi = 1$, “partially stuck” for $0.0 < \phi < 1.0$, and “creeping” for $\phi = 0$ (the word stuck implies less permanency than does locked). In most cases, ϕ is neither 0 nor 1, which is interpreted as a spatial average of

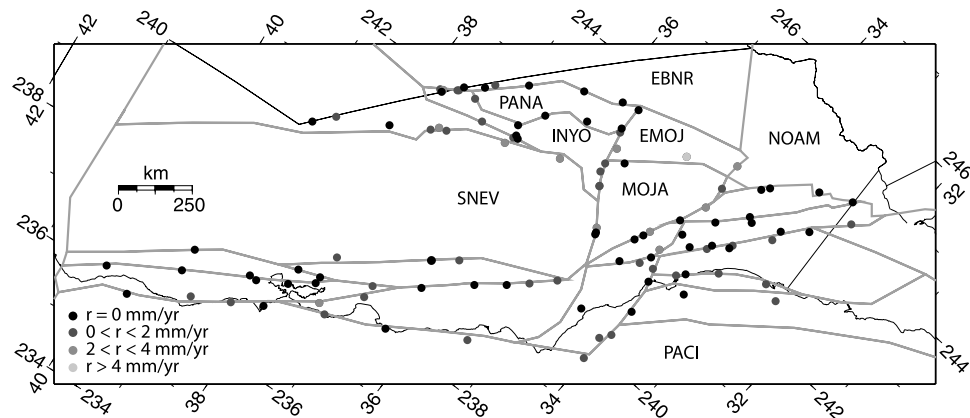


Figure 4. Fits to geologic fault slip rates; r represents how much the calculated slip rate fell outside the range of observed rate. Coloring of dots shows the level of agreement. See color version of this figure in the HTML.

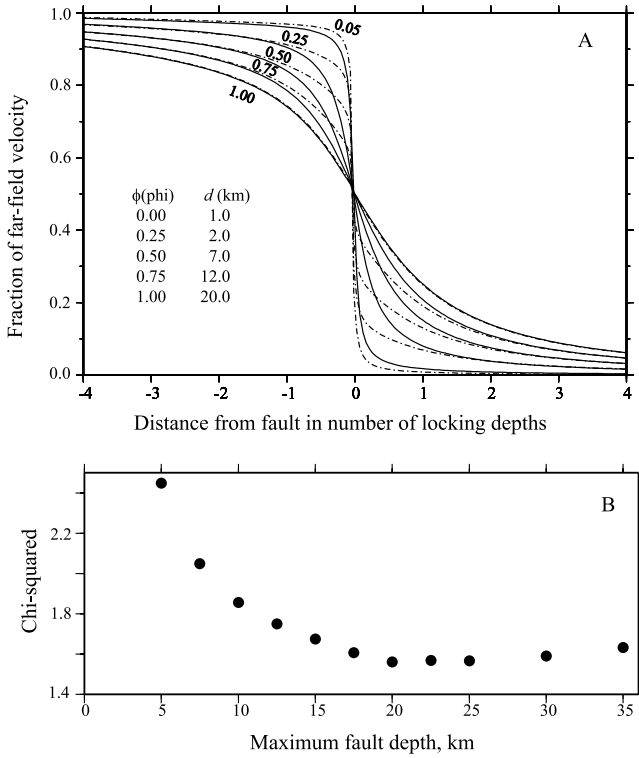


Figure 5. (a) Comparison of the predicted fault-parallel velocities from the fault parameterization used here to the more common “fixed locking depth” method. Solid curves show velocity profiles across a vertical strike-slip fault with locking depths of $0.05d$, $0.25d$, $0.50d$, $0.75d$, and $1.00d$ (as labeled), where d is a reference depth. In this case the fault is fully stuck from the surface to the locking depth. Dashed curves show velocity profiles when the fault is fully stuck from the surface to depth $0.05d$ and then partially stuck at a fraction ϕ down to depth d (labels refer to ϕ). The table gives an approximate correlation of ϕ with the locking depth method. (b) Plot of overall reduced χ^2_n relative to the assumed maximum depth of the sticking on faults. For a given maximum fault depth, full creep occurs below it, and partial creep can occur above. On the basis of this a maximum fault depth of 20 km was used.

creeping and stuck patches on the fault surface [Scholz, 1990; McCaffrey *et al.*, 2000; Lay and Schwartz, 2004].

[19] The component of the slip vector on a fault that gives rise to the elastic deformation around the fault is therefore $\phi \mathbf{V}$ where \mathbf{V} is determined from the angular velocities and permanent strain rates of the blocks that are in contact at the fault (the product $\phi \mathbf{V}$ is often called the “slip rate deficit”). The scalar ϕ is subject to the constraint $0.0 \leq \phi \leq 1.0$ which assures that the fault slip and resulting elastic strain rates are kinematically consistent with the block rotations and permanent strain rates. Surface deformation due to a stuck fault is then estimated by applying back slip at a rate of $-\phi \mathbf{V}$.

[20] A commonly used approach to estimating fault behavior is to assume the fault is stuck (no creep) from the surface to a depth d (the “locking depth”) and creeping below that. In the inversions here, faults are prevented from

creeping at the near-surface ($\phi = 1$ at $z = 0$) and a uniform value of the free parameter ϕ is estimated for the 1 to 20 km depth range on the fault. (ϕ decreases from 1.0 at the surface to an estimated value ϕ_e at 1 km depth, remains at ϕ_e down to the bottom of the fault at 20 km depth, and below 20 km the fault creeps, i.e., $\phi = 0$.) This approximation is similar to using the locking depth concept but has the advantage in that the parameter ϕ is linearly related to the surface deformation, allowing the use of a spatial convolution to calculate forward models. In Figure 5a the expected fault-parallel velocities for a series of values of ϕ are compared to the locking depth equivalents. Farther than about 1 locking depth from the fault the equivalent locking depth d is approximately equal to ϕd_o , where d_o is the maximum depth to which any fault can be stuck. However, it is also evident in Figure 5a that strain rates are more localized near the fault for my approximation, indicating that the equivalent locking depth d will be less than or equal to ϕd_o . For a vertical fault and using $d_o = 20$ km, the slip rate fraction ϕ roughly corresponds to an equivalent locking depth d as shown in Figure 5a. For long faults, ϕ is allowed to vary along strike.

[21] For every fault in the structural model, nodes are placed at the surface, 1 km depth, and 20 km depth. The choice of 20 km for this bottom depth (d_o) was arrived at by testing d_o at values ranging from 5 to 35 km in and examining the data misfits (Figure 5b). At $d_o = 20$ km and deeper, the χ^2 does not change significantly while shallower depths produce larger misfits – hence $d_o = 20$ km is used. This result does not mean that the best locking depth is 20 km but instead suggests that there is likely predominantly creep below 20 km depth on all of the faults in the model.

3. Results

[22] Several inversions were performed initially to identify which types of parameters were required to match the observations. An inversion that includes only elastic rotating blocks and faults (no permanent strain within blocks) has a reduced chi-square (χ^2_n) statistic of 1.56 (all runs described here include free parameters for the rotations of the 11 GPS velocity fields into the North America frame). This inversion has 3139 degrees of freedom (dof): 3288 observations and 149 free parameters (three parameters each for the angular velocities of 20 blocks and 11 velocity fields plus 56 fault parameters). When, in addition, permanent strain rates within 19 blocks are estimated, 57 additional parameters are used (three for each block, excluding NOAM and PACI) and $\chi^2_n = 1.24$. A run in which all blocks rotate and strain uniformly but all faults creep (all $\phi = 0$) produces $\chi^2_n = 4.97$, which has a probability $P < 10^{-150}$ of being as good a fit to the observations as the case that includes variable creep on faults. Such tests show that a model in which the deformation field is composed of uniformly straining regions bounded by fully creeping faults does not satisfy the observations. As also shown by Wdowinski *et al.* [2001], these results indicate that the highest modern strain rates in the western United States are largely associated with known faults.

[23] Similarly, inversions in which all faults are held fully stuck (all $\phi = 1.0$, 99 free parameters, $\chi^2_n = 2.86$) or fully

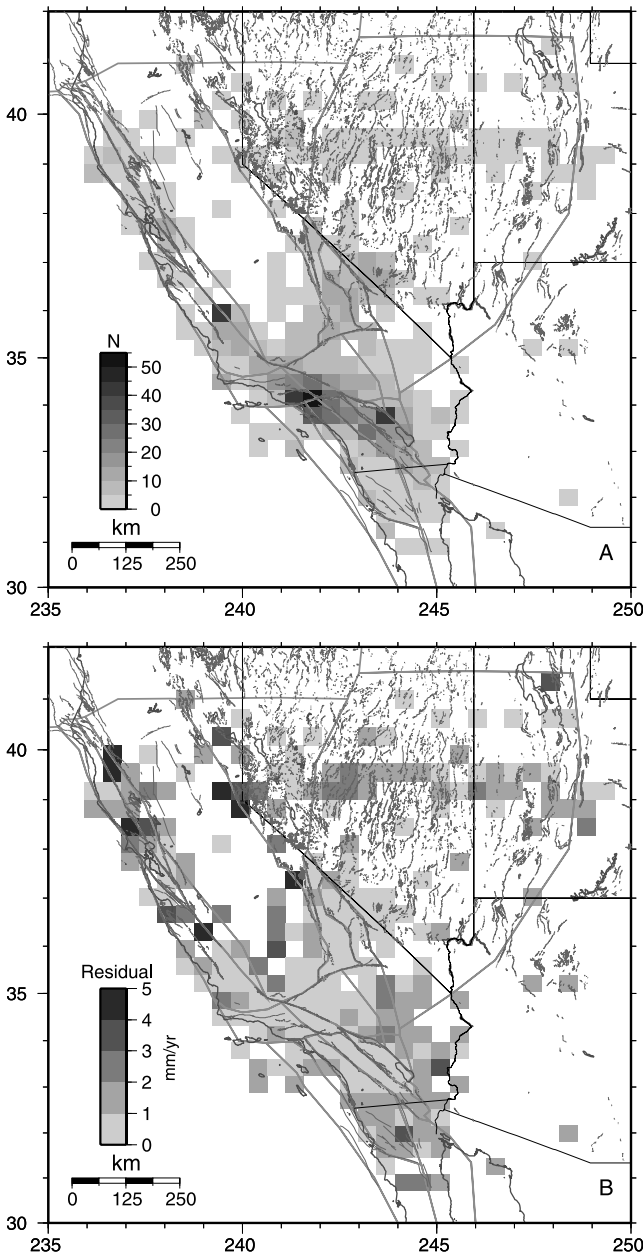


Figure 6. Map representing GPS velocity residuals. (a) The number (N) of GPS observed velocities within a grid of $40 \text{ km} \times 40 \text{ km}$ regions. Unshaded areas have no GPS observations. (b) Lengths of the weighted averages of the residuals calculated in same $40 \text{ km} \times 40 \text{ km}$ regions. The scalar value used is $\{\sum_N (r_e \sigma_e^{-2}) / \sum_N \sigma_e^{-2}\}^2 + [\sum_N (r_n \sigma_n^{-2}) / \sum_N \sigma_n^{-2}\}^2\}^{1/2}$, where r_e and r_n are the east and north velocity residuals, σ_e and σ_n are the east and north velocity uncertainties, and the summation is over N , the number of velocities in the region. See color version of this figure in the HTML.

creeping (all $\phi = 0.0$, 99 free parameters, $\chi_n^2 = 5.77$) while allowing block rotations only have $P < 10^{-200}$ of being as good a fit to the observations as variable fault creep models, indicating the need for spatial variations in creep on faults. In summary, the tests indicate that a combination of block rotations, fault induced elastic strain, and some regions of

permanent strain are needed to match the kinematic data. As will be discussed, inversions in which each block alone is allowed to strain internally (along with faulting and rotation parameters) are used to examine the necessity of including permanent strain rates. The improvements in the fits by allowing uniform permanent strain rates varied from block to block. However, more than 80% of the total variance reduction achieved by allowing strain in all 19 blocks is realized from only eight of them. Hence the preferred set of parameters is one in which permanent strain rates are included in eight of the blocks, producing $\chi_n^2 = 1.29$.

[24] The fits to the three data types are within expected levels of uncertainty (Table 2). The 3046 GPS velocity components are fit at NRMS = 1.12 and WRMS = 1.0 mm/yr while individual velocity fields are fit with NRMS ranging from 0.88 to 1.31 (Table 1). The WRMS of the individual velocity fields range from 0.6 mm/yr for MC01 [McCluskey *et al.*, 2001] and BEAV [Beavan *et al.*, 2002] to 2.4 mm/yr for the northern California velocity field JF99 [Freymueller *et al.*, 1999]. The largest misfits to the GPS velocities are generally near faults but only in a few localized cases (Figure 6).

3.1. North American Reference Frame

[25] A major issue in interpreting GPS-derived surface velocities is the appropriate reference frame. Many researchers identify GPS sites that they think should be fixed relative to the reference frame (e.g., not in deforming areas) and from them estimate a transformation to minimize velocities. Because the approach used here accounts for elastic and permanent deformation, GPS vectors are not removed due to their proximity to faults, resulting in angular velocity estimates from a broader geographical distribution of data. The two velocity solutions that are presented in the IRF2000 reference frame [Boucher *et al.*, 2004; Beavan *et al.*, 2002] give similar rotations for North America in that frame (Table 1). For example, the differences in the observed velocities at site VNDP in California rotated into the NOAM frame are 0.1 mm/yr in East and 0.2 mm/yr in North. Since most of the remaining fields are originally published in some realization of the North America frame, their adjustments to the NOAM frame are generally less than 1 mm/yr . Exceptions are the JF99 [Freymueller *et al.*, 1999] velocities given in the Pacific reference frame and the MC01 [McCluskey *et al.*, 2001] velocities given relative to a site within the network. The adjustment to the SCEC CDM3 velocity field (CMM3) was about 0.1 mm/a in the south and 0.3 mm/yr eastward. In all, 222 GPS velocities defined the NOAM plate misfit NRMS = 1.15 and WRMS = 0.9 mm/yr (Table 3). (Adjustments to the NOAM reference frame for each site are given in the auxiliary material.)

3.2. Pacific–North America Motion

[26] The best fitting angular velocity describing the rotation of the Pacific plate relative to North America is very close to that estimated by Beavan *et al.* [2002] and DeMets and Dixon [1999] but different from other published estimates (Figure 7a). This new pole satisfies the 0.78 Ma PACI-NOAM spreading rate published by DeMets [1995], five Gulf of California transform azimuths, 72 earthquake slip vector azimuths, and 55 GPS velocities on

Table 3. Fits to GPS Velocities for Each Block and the Blocks' Rotation Poles^a

Block	Code	<i>N</i>	NRMS	WRMS	SumWt	Longitude	Latitude	Omega	Sig Omega	Max	Min	Azimuth
Anza	ANZA	206	1.03	1.1	167	281.37	49.60	-0.681	0.279	20.9	0.5	253.8
Catalina	CATA	54	1.02	1.1	44	313.16	49.31	-0.517	0.104	21.7	0.5	101.5
Eastern Baja	EBAJ	26	0.94	1.1	18	275.60	47.25	-0.811	0.298	15.8	0.6	247.7
Eastern Basin and Range	EBNR	320	1.02	0.9	454	241.12	26.08	0.132	0.022	3.2	0.7	12.6
Eastern California Coast Ranges	ECCR	28	1.22	1.1	33	281.71	51.11	-0.328	0.251	38.0	0.8	264.0
Eastern Mojave	EMOJ	68	1.34	1.1	103	248.25	40.07	-0.580	0.333	5.0	0.5	219.3
Great Valley thrust belt	GVTB	82	1.23	1.2	91	245.19	40.55	-1.231	0.656	4.5	0.3	230.0
Inyo	INYO	116	0.94	0.6	246	246.82	40.67	-0.650	0.199	2.4	0.3	222.9
Northern Mojave	MOJA	174	1.12	1.1	193	213.03	6.11	0.218	0.226	57.3	1.1	39.3
North America	NOAM	444	1.15	0.9	803							
Pacific	PACI	110	1.28	1.0	175	284.16	50.19	-0.761	0.003	0.2	0.2	263.7
Panamint	PANA	58	0.82	0.7	82	245.86	39.52	-0.618	0.294	2.7	0.4	223.5
Salinian	SALI	188	1.08	1.2	166	260.77	47.07	-1.240	0.268	6.3	0.2	242.4
Salton	SALT	208	1.02	1.1	168	311.54	46.84	-0.314	0.348	77.3	1.4	101.2
Santa Ana	SANA	48	1.10	1.3	34	264.65	46.75	-1.098	0.360	10.5	0.4	240.3
San Gabriel	SGAB	82	1.19	1.3	71	265.70	49.37	-0.903	0.858	31.3	0.5	238.5
Southern Mojave	SMOJ	64	1.15	1.4	42							
Sierra Nevada	SNEV	172	1.37	1.1	249	256.93	50.72	-0.384	0.037	2.5	0.3	230.0
SW Mojave	SWMO	4	0.43	0.6	2	223.60	23.81	0.258	3.136	109.4	2.3	55.3
Ventura (Transverse Range)	VENT	248	1.26	1.3	216	269.57	48.91	-0.899	0.308	13.2	0.3	246.5
Western Baja	WBAJ	200	0.96	1.1	160	268.15	47.50	-0.928	0.160	6.1	0.3	243.2
Western California Coast Ranges	WCCR	60	1.13	1.3	48	262.50	47.82	-0.703	0.232	10.0	0.4	250.2
Western Basin and Range	WEBR	86	1.14	0.9	130	250.87	47.82	-0.385	0.089	3.7	0.3	224.1

^a*N* is the number of data in the block, twice the number of vectors for GPS data; SumWt is the sum of the weights for the velocities; Latitude, Longitude, and Omega give the Euler pole for the block rotation relative to North America; Sig Omega is the uncertainty in the rotation rate (degrees Ma); Max, Min, and Azimuth are the 68% confidence error ellipse for the block rotation.

the Pacific plate. Because of the addition of data not used by others the formal uncertainties in the new Pacific–North America angular velocity are smaller (Figure 7a). The 55 GPS velocities on the Pacific plate are fit with NRMS = 1.28, WRMS = 1.0 mm/yr.

[27] GPS vectors from coastal California sites that are likely on the Pacific plate are normally excluded from pole estimations due to the influence of elastic strain near faults [e.g., Beavan *et al.*, 2002]. The inversion used here optimally estimates the elastic strain rate component and these data are retained. Beavan *et al.* [2002] noted that four sites along coastal California were inconsistent with Pacific motion in the North America frame at the 4–5 mm/yr level. They showed that three of them could be satisfied by including elastic strain rates from nearby faults but that one, SNI1 on San Nicholas Island (Figure 8a), could not. The fits to these sites and nearby ones on the Pacific plate from this inversion are shown in Figure 8. In southern California the residual for Beavan *et al.*'s SNI1 velocity (2.0 ± 0.6 mm/yr) (uncertainties quoted on rates are one-dimensional, one-sigma values) is still outside the 95% confidence ellipse yet the fits to the CMM3 velocity estimates at SNI1 (1.5 ± 1.0 mm/yr) and at nearby site TWIN (1.7 ± 0.9 mm/yr) are both within this limit (Figure 8a). In Northern California (Figure 8b), Beavan *et al.*'s FARB velocity is not fit at 95% level (2.3 ± 0.6 mm/yr) while the BARD [Murray and Segall, 2001] velocities for FARB (0.7 ± 0.7 mm/yr) and nearby sites are matched. GPS velocities from the 11 Beavan *et al.* Pacific Basin sites (Figure 8c) are fit with a reduced χ^2 of 1.1 compared to their value of 0.9 (with only 19 dof this level of change has a 66% chance of being random).

3.3. Profiles Across the Deforming Zone

[28] Profiles of the observed and calculated GPS velocities (Figure 9) crossing the western United States

show that the kinematic model can reproduce the GPS velocities across the entire margin starting on the Pacific plate in the west all the way to the North American plate in the east. The west ends of the profiles show that predicted Pacific motion, modified by strain rates on boundary faults, is consistent with the westernmost GPS velocities. Hence the new PACI-NOAM angular velocity satisfies data from both the far-field and the deforming zone.

[29] The inversion in general produces a stepwise decrease in the long-term tangential block velocities relative to North America from west to east (Figure 9, right; profiles 1–6 are along lines radiating from the PACI-NOAM pole). In addition, the radial velocities are generally small indicating that the blocks move largely parallel to predicted PACI-NOAM motion. The inversion does not in any way require these features as the blocks are free to rotate about any axis passing through the center of the Earth. Hence the kinematic data from the western United States indicate very little excess rotation of the blocks. Rotations will be discussed in detail later in the paper.

3.4. Fault Creep Rate Estimates

[30] The inversion estimates the distributions of creep rates on all faults that separate blocks (Figure 10). As noted earlier, the parameter ϕ is the fraction of the fault slip rate which is stuck across the fault (i.e., one minus the fraction of steady creep). Test inversions discussed earlier showed the necessity of including spatially variable fault creep to fit the observations. In the inversion, nodes along strike of a fault segment can be forced to have the same value of ϕ ; this constraint decreases the formal uncertainties in the value of the free parameter ϕ at the expense of the spatial resolution of the creep. For most faults, the distribution of the nodes and their spatial interdependence were adjusted to keep the formal uncertainties in ϕ less than 0.3 though some short fault segments have uncertainties up to 0.5.

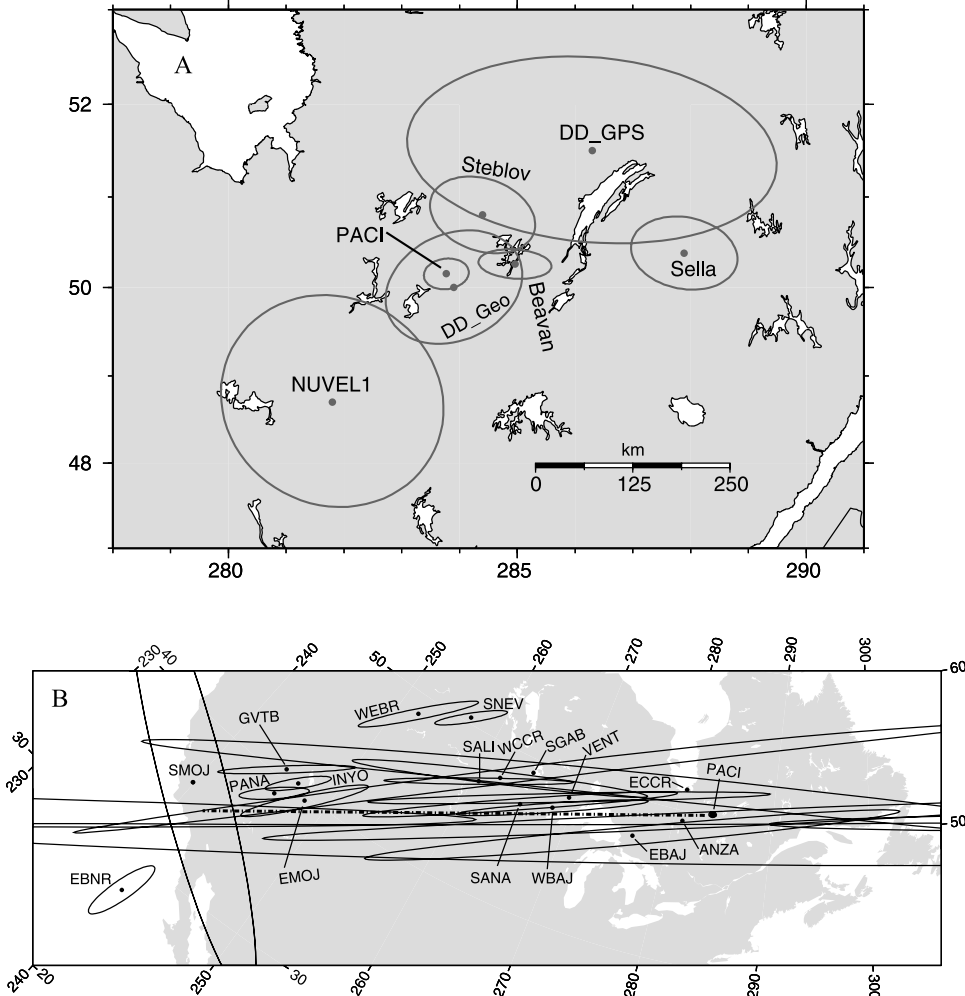


Figure 7. (a) Pacific–North America rotation poles and their error ellipses. The poles are labeled as NUVEL1 [DeMets *et al.*, 1994], DD_Geo and DD_GPS (the geological and GPS-based poles of DeMets and Dixon [1999]), Steblow [Steblov *et al.*, 2003], Beavan [Beavan *et al.*, 2002], and Sella [Sella *et al.*, 2002]. The “PACI” pole is estimated in this study. (b) Poles of rotation for western United States blocks relative to North America in oblique Mercator projection along great circle (dashed line) connecting California to the PACI-NOAM pole (labeled PACI).

[31] The inferred creep on the faults estimated through the parameter ϕ is primarily used to account for elastic strain. The particular value of ϕ will depend on details of the fault, such as dip angle and exact position of the fault, that are not in detail well represented by this structural model. Hence it is probably unwise to overly interpret the estimated variations in ϕ . Nevertheless, it is notable that the inversion was able to detect the known creeping regions along the San Andreas north of Parkfield and along the southern Calaveras fault near Hollister (Figure 10). Additional information on the faults is provided in the auxiliary material.

3.5. Fault Slip Rates

[32] In general there are no large systematic misfits to fault slip rates except in the Mojave region. Observations that have large residuals often have nearby well-fit observations (Figure 4). The NRMS misfit of 0.86 for the fault slip rates indicates that the rates predicted by the relative

motions of the blocks are in most cases within the assigned uncertainties of the geologic rates. Figures 3a and 3b show the predicted fault slip vectors and observed and predicted slip rates for the best model. Clearly, the dominant fault is the San Andreas. Slip on the San Andreas is parallel to the fault throughout most of its length; exceptions are along the mountainous San Gabriel–Mojave segment (Figure 3b), where some fault-normal contraction is predicted.

3.5.1. Southern Mojave Region

[33] The largest misfits between observed and calculated long-term fault slip rates occur in the southern Mojave region of southern California. The GPS velocities there may be subject to transient behavior associated with recent earthquakes but are not driving this misfit.

[34] In the region of the southern Mojave Desert (SMOJ block) south of the Pinto Mountain fault (PMF) and east of the San Andreas fault (SAF), the generally accepted [Working Group on California Earthquake Probabilities, 1995] fault slip rates on the San Andreas

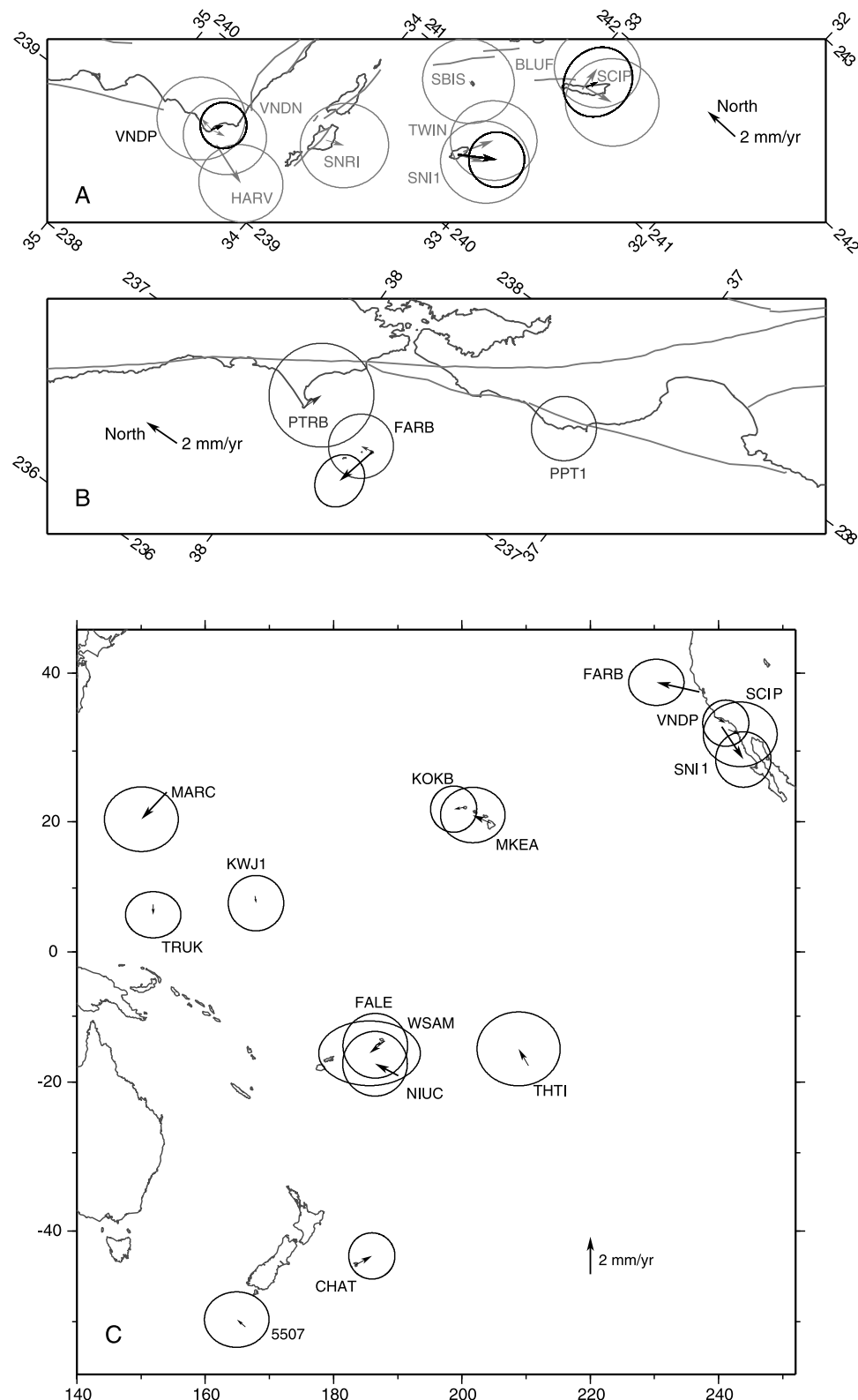


Figure 8. (a and b) Residual velocities for GPS sites on the Pacific plate with 95% confidence ellipses. In Figure 8a, gray vectors are from SCEC Crustal Motion Map CMM3 solution, and black vectors are from Beavan *et al.* [2002]. In Figure 8b, the longer FARB vector is from Beavan *et al.* [2002], and others are from BARD [Murray and Segall, 2001]. (c) Residuals for Beavan *et al.* Pacific vectors relative to new Pacific–North America pole.

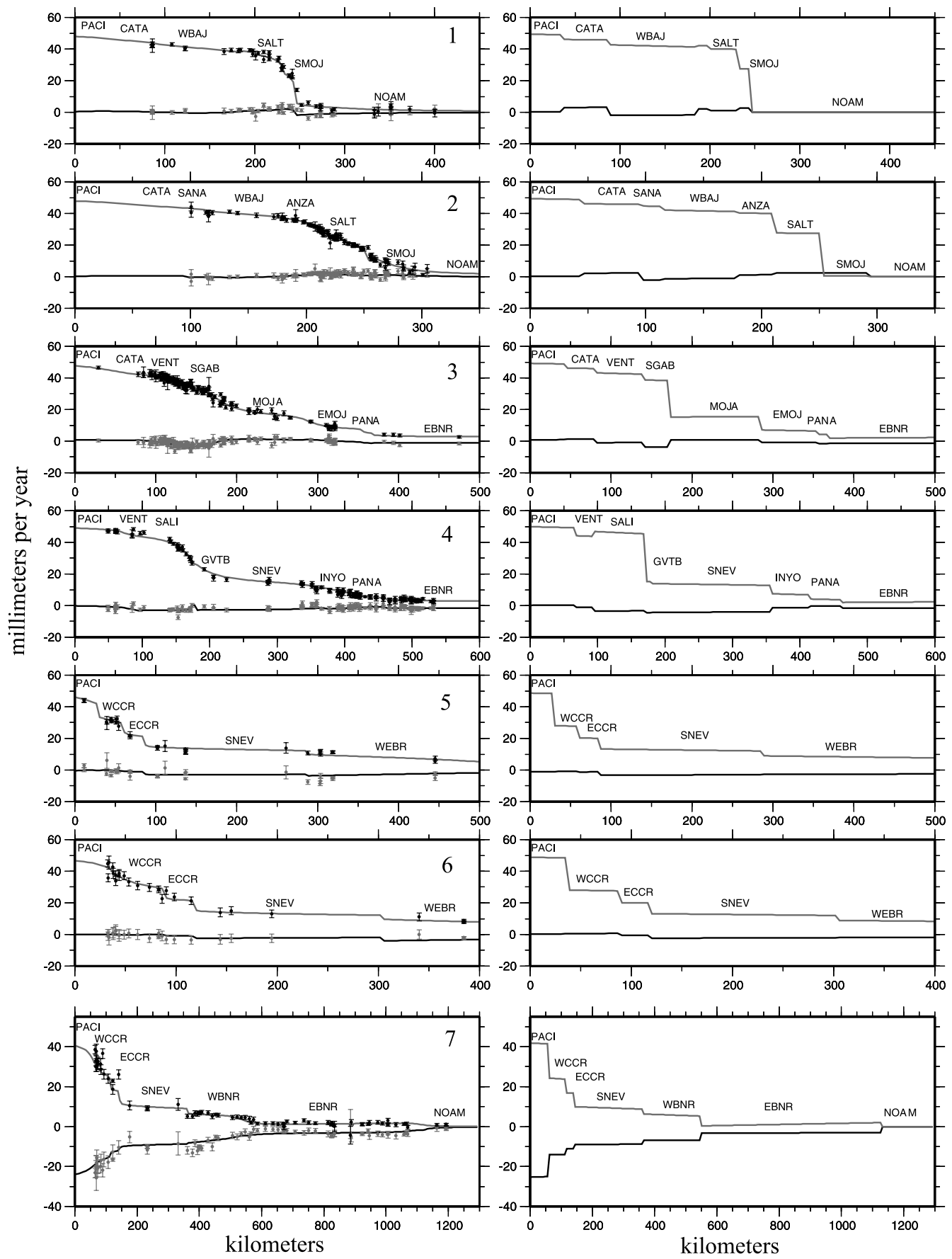


Figure 9

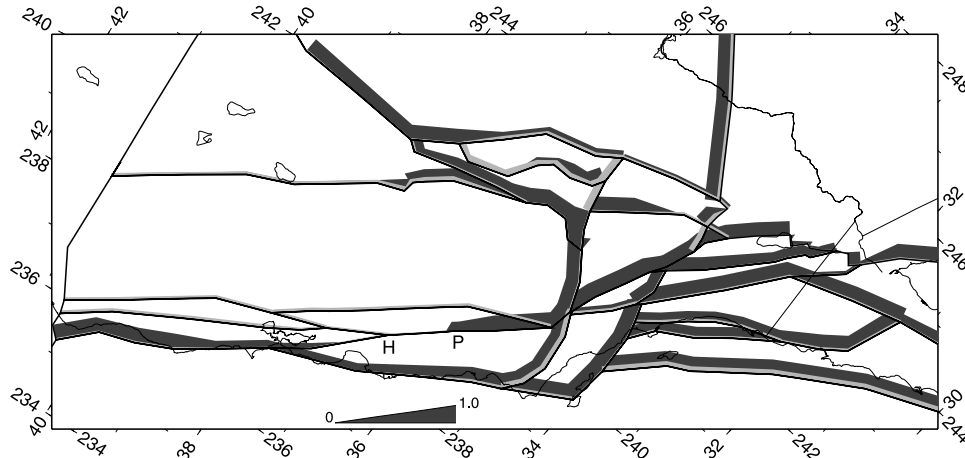


Figure 10. Fault creep estimates. The values of ϕ (1.0 minus the creep fraction) are projected along the faults (scale at bottom). Black shows the value of ϕ , and gray shows the uncertainty in ϕ . H and P show the locations of Hollister and Parkfield; ϕ drops dramatically north of Parkfield, indicating significant creep.

(20 to 30 mm/yr) and the San Jacinto (6 to 18 mm/yr) combine to make up most of the required Pacific–North America motion and hence indicate that the SMOJ block (Figures 11a and 11b) moves slowly relative to North America. No obvious faults that would allow rapid motion of SMOJ relative to NOAM have been mapped and GPS velocities in the SMOJ block likewise indicate little motion relative to North America. Inversions in which SMOJ is allowed to move relative to NOAM result in little motion (<3 mm/yr) across the implied boundary (Figures 11a, 11b, 11c, and 11f). Other inversions in which SMOJ is constrained to move with NOAM do not result in significant misfits (Figures 11d and 11e).

[35] The rapid (\approx 15 mm/yr) northwestward velocity of the Mojave (MOJA) block evident in GPS velocities requires nearly equally rapid extension on the Pinto Mountain fault (PMF) if that fault alone separates the MOJA and SMOJ blocks (Figures 3b, 11a, and 11b). The PMF is thought to accommodate 0.3 to 5.3 mm/yr of left-lateral strike slip [Wesnousky, 1986], but Dokka and Travis [1990] show extension in their block model of the region. Both Dokka and Travis [1990] and Humphreys and Weldon [1994] called on block rotations south of the PMF to help accommodate NW motion of the southern Mojave region but this can add only a small amount.

[36] Figures 11c–11f show possible alternatives for the block geometry in the southern Mojave region. Inversions using the block geometries shown in Figures 11d–11f result in distribution of the slip on both the Pinto Mountain and Eureka faults (EPF). The Eureka Peak fault (Figure 11d) extends south of the PMF and ruptured in the 1992 Landers earthquake but has an unknown slip rate. The models in

which the southern Mojave block is divided along the EPF (Figures 11d–11f) produce more reasonable rates of slip on the PMF but predict a probably unreasonably large right-lateral slip rate of up to 10 mm/yr along the EPF. At this point, using a large-scale block model, the relative motion of the Mojave and southern Mojave blocks cannot be satisfactorily reconciled with estimates of geologic slip rates.

3.5.2. Eastern California Shear Zone

[37] The eastern California shear zone (ECSZ) accommodates motion of the Sierra Nevada (SNEV) block relative to the Basin and Range (EBNR). At latitude 36° N the relative motion across the ECSZ is 11.3 ± 0.3 mm/yr at azimuth $308^{\circ} \pm 1^{\circ}$ based on the SNEV and EBNR poles (the Pacific–North America azimuth is $322^{\circ} \pm 1^{\circ}$ here). This rate is nearly identical to that estimated by McCluskey *et al.* [2001], though theirs was based on a more limited geographical distribution of GPS sites.

[38] The azimuth of the ECSZ is about $320^{\circ} \pm 5^{\circ}$, very close to the PACI–NOAM azimuth (see Figure 3a) and about 10° clockwise from the SNEV–EBNR azimuth. The relative azimuths indicate predominantly right-lateral strike slip across the ECSZ except where releasing bends cause oblique extension. This agrees with the analysis of Unruh *et al.* [2003], who suggested that the ECSZ fault pattern reveals NW motion of the Sierras relative to North America. Strictly speaking, these faults accommodate motion of SNEV relative to adjacent blocks to the east (Figure 1), not relative to NOAM. Conceptually, the results here agree with the findings of Unruh *et al.* [2003] that the ECSZ fault slip is accommodating shear and the extension occurs at releasing bends in the fault systems.

Figure 9. (left) Observed and calculated GPS velocities along profile lines 1 through 7 shown in Figure 2a. Gray lines and black symbols show component of velocity normal to profile line (N or NW is positive). Black lines and gray symbols show velocity component parallel to profile line (E or NE positive). Symbols are GPS velocities that fall within 30 km of the profile projected onto the profile azimuth, with one standard deviation error bars. (right) Block velocities (gray for components normal to profile, black for component parallel to profile). Block names given above the curves show where the profile crosses the block.

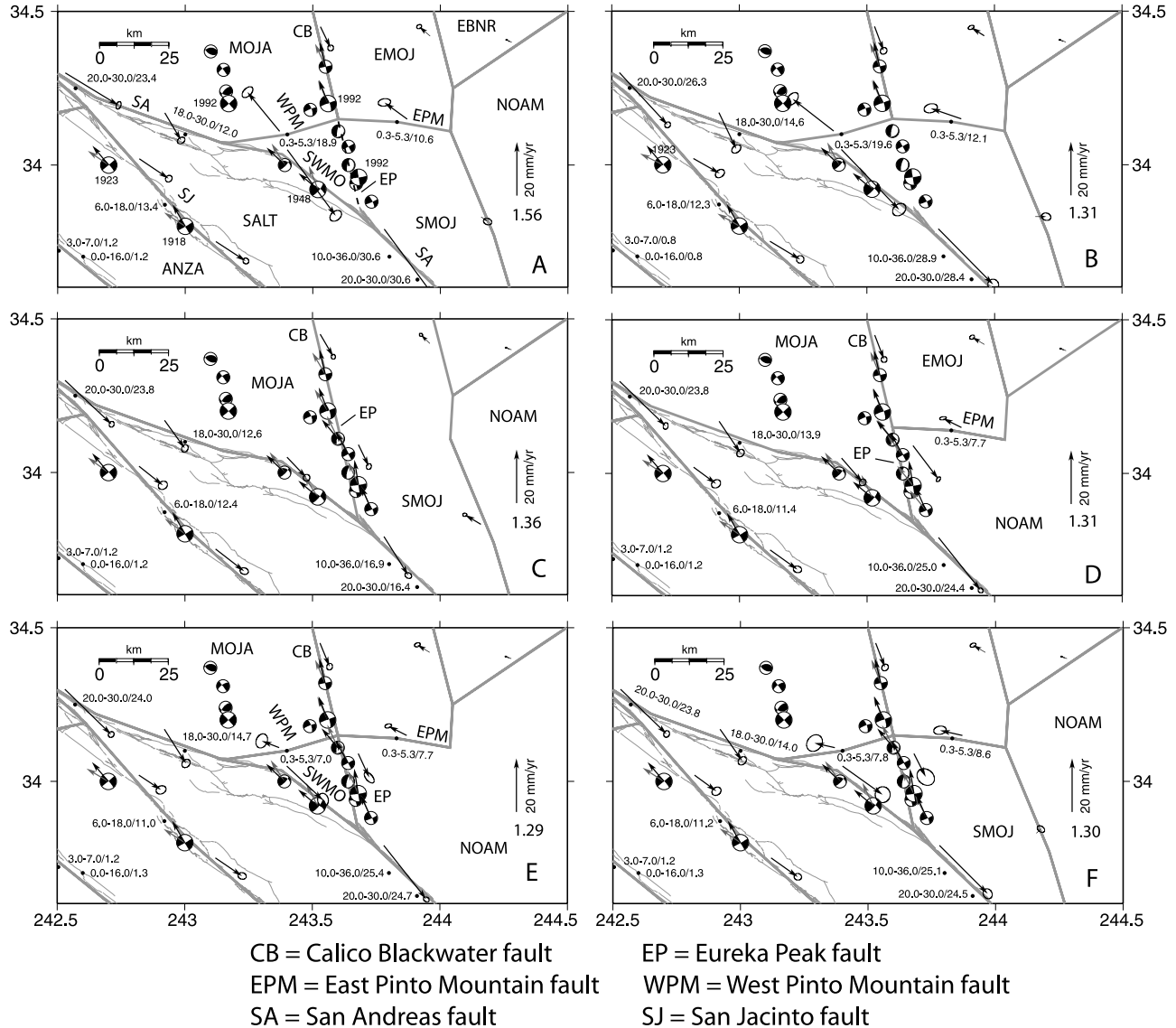


Figure 11. Alternative block geometries for the Mojave region. Number under the velocity scale shows χ^2_n for the model. Labels are as in Figures 3a and 3b. (a) No strain in blocks. Motion of Mojave (MOJA) relative to southern Mojave (SMOJ) occurs by slip on Pinto Mountain fault. (b) Geometry as in Figure 11a but permanent strain rates allowed in blocks. (c) Slip between MOJA and SMOJ occurring along Eureka Peak fault (EP) as southern extension of Calico-Blackwater fault (CB). (d) Slip allowed on Eureka Peak and East Pinto Mountain faults; SE Mojave (SMOJ) part of North America (NOAM). (e) As in Figure 11d but slip allowed on West Pinto Mountain fault also. (f) Slip allowed on East and West Pinto Mountain faults, Eureka Peak fault, and SW Mojave (SWMO) moves relative to North America. The scenario in Figure 11e fits the observations best but indicates rapid slip on the Eureka Peak fault.

[39] Dixon *et al.* [2003], and others cited therein, note that geodetic-derived fault slip rates from the western ECSZ systematically overestimate geologically estimated rates on the same faults. In particular, the Owens Valley–Airport Lake (OV-AL) fault, which has an estimated geologic rate of 2.6 ± 0.5 mm/yr [Beanland and Clark, 1994], is commonly assigned rates of 5–7 mm/yr when matching GPS velocities alone. Dixon *et al.* attribute this difference to bias in the GPS velocities due to unmodeled transient effects of a viscoelastic medium. The inversions here give a slip rate of 5.9 ± 0.5 mm/yr on the OV-AL fault at 36°N .

[40] Tests reveal other possibilities for the disagreement between GPS velocities and the geologic slip rate on the OV-AL fault. First, inversions in which the slip rate at 36°N is tightly constrained to a series of values reveal that most kinematic data favor a higher slip rate on the OV-AL fault; only the slip vector azimuths are fit best at a rate of 4 mm/yr (Figure 12a). Fault slip rate data as a whole also prefer a rate of 5 to 6 mm/yr on the OV-AL fault. This suggests that perhaps the estimated geologic slip rate on the OV-AL fault is underestimated or more unidentified faults are slipping. A second scenario that results in lower slip rates on the OV-AL

fault is the inclusion of strain within the INYO block (Figures 12b–12d). This lowers the predicted slip rate to 4.3 ± 0.5 mm/yr and again can be interpreted as slip on other faults.

3.5.3. Great Valley Thrust Belt

[41] The Great Valley thrust belt shows nearly pure thrusting in the south in the vicinity of the 1983 Coalinga

thrust quake (Figure 3a) and becomes more right-lateral in the north. The estimated slip rate is about 3.4 to 3.6 mm/yr along its length, similar to shortening rates estimated by Namson and Davis [1988], Sauber et al. [1989], and Argus and Gordon [2001]. The block itself appears to be straining internally at a rapid rate with NE directed contraction (Figure 13).

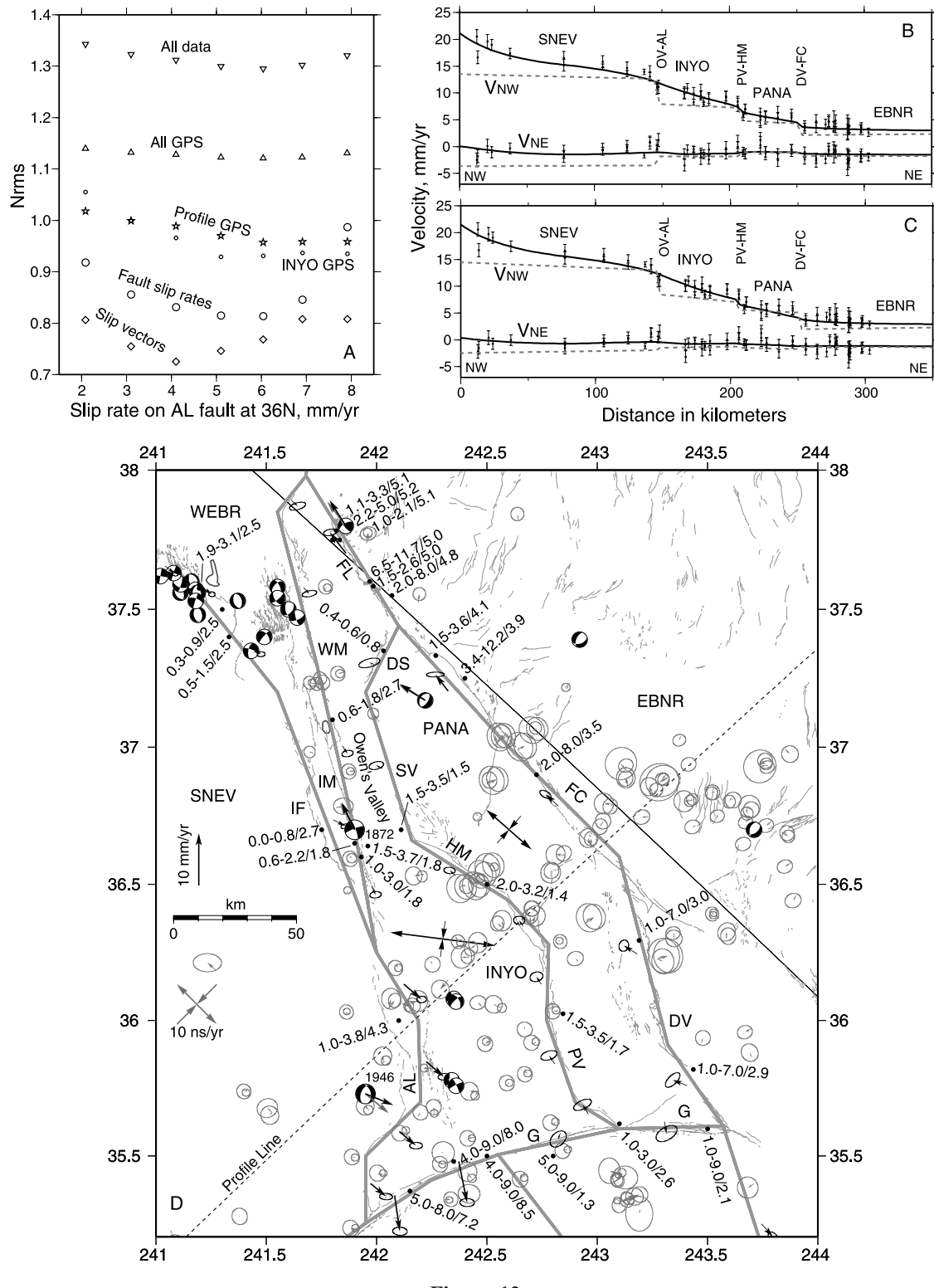


Figure 12

3.5.4. Bay Area, California

[42] The block model satisfies GPS velocities, fault slip rates, and earthquake slip vectors in the San Francisco Bay Area, a complex interaction of faults (Figure 3a). Predicted slip directions remain largely parallel to the major faults except on the San Andreas east of Monterey Bay where a component of fault-normal convergence is seen. However, the slip vector azimuth of the 1989 Loma Prieta earthquake (LP in Figure 3a) is matched within a few degrees showing the block motions are consistent with oblique slip on that section of the San Andreas.

3.5.5. Coastal California

[43] A few mm/yr of right-lateral and convergent slip are predicted for offshore faults south of Monterey Bay. The Hosgri fault includes a component of convergence which may account for the recent San Simeon thrust earthquake near it (SS in Figure 3a).

[44] In northern coastal California, geologic fault slip rates are well matched on the San Andreas (SA), Ma'acama–Rogers Creek (Ma-RC), and Bartlett Springs (BS) faults (Figure 3a). The predicted slip vectors on the Ma-RC and BS faults indicate largely right-lateral slip with minor amounts of convergence, consistent with seismicity [Castillo and Ellsworth, 1993]. Predicted slip rates on the faults are somewhat different from those estimated by Freymueller *et al.* [1999]. They predicted nearly equal slip rates on the SA (14.3 to 19.5 mm/yr) and Ma-RC (11.1 to 18.0 mm/yr) faults while this inversion results in rates of 20.9 ± 0.7 and 7.3 ± 0.9 mm/yr, respectively. We get similar rates for the BS fault (their 6.3 to 10.3 mm/yr compared to my 7.3 ± 0.7 mm/yr). The differences in the SA and Ma-RC slip rates likely result from including geologic slip rates as constraints in this inversion, from having additional GPS observations in northern California, and from the block model requiring that the fault slip rates satisfy data from the Bay Area as well as from northern California. The GPS observations of Freymueller *et al.* [1999] are fit at NRMS = 0.88 by the block model.

4. Permanent Strain Rates Within Blocks

[45] The long-term elasticity of the blocks is tested by estimating uniform, horizontal strain rate tensors within each block in addition to the elastic strain rates induced by faults. The uniform strain rates, which are not consistent with the expected pattern of elastic strain rates, are assumed to represent nonrecoverable strain rates within the block and are therefore called “permanent” here. The combination of elastic and permanent strain rates can result from a macro-

scale elastic-plastic rheology sometimes used to represent continental deformation [Peltzer and Tapponnier, 1988].

[46] Permanent strain rates as defined above are estimated in two ways: (1) derived from velocity residuals for a run in which only block rotation and fault locking are allowed (Figure 13a) and (2) adjusted simultaneously with fault locking and block rotation as part of the inversion (Figure 13b). The estimates made by the two approaches are in general similar but differ because the inclusion of permanent strain rates in the formal inversion requires them to match observations other than the GPS velocities. For example, internal permanent strain rates in a block will change the predicted slip rates and azimuths on block-bounding faults.

[47] The percent reduction in the total misfit χ^2 resulting from the inclusion of 3 uniform strain rate parameters for each of the western United States crustal blocks (excluding NOAM and PACI blocks) is 22% (from 4900 to 3833). To determine which blocks contribute most to the variance reduction, inversions were done in which one block at a time has permanent strain estimated and the variance reduction is calculated. Nearly half of the total variance reduction comes from three blocks (GVTB, VENT and SALT) (Figure 13c). The VENT block, which contains the Transverse Ranges, shows nearly uniform NNE directed contraction, normal to the faults. Including strain in three more blocks (MOJA, ANZA and SALI) that each alone has more than 1% variance reduction accounts for two thirds of the total variance reduction. Over 80% of the variance reduction results from strain rates in only 8 of the 20 blocks (the six above plus WEBR and SGAB; Figure 13c).

[48] For the decrease in the number of degrees of freedom (from 3139 to 3136) resulting from adding the three free parameters for a permanent strain rate tensor, a 1% reduction in variance has a 39% chance of being random (a 0% variance reduction has a 50% chance of being random). Hence, for most of the blocks, where the variance reduction is less than 1%, the permanent strain rate parameters do not improve the data fit significantly. Permanent strain rates in the two largest blocks, EBNR and SNEV, each produce less than 0.5% variance reduction, corresponding to a 44% chance of being random. Moreover, the inversions result in principle strain rates of less than 3 nanostrain/yr in both blocks.

[49] The 6 blocks that produce two thirds of the variance reduction resulting from allowing permanent strain rates comprise less than 10% of the area of the deforming zone while the 8 blocks that produce more than 80% of the

Figure 12. Tests of fault slip rates in the eastern California shear zone (ECSZ). (a) Misfits to various subsets of the data plotted against slip rates imposed on the Airport Lake (AL) fault at 36°N . Points labeled “All data” give the χ^2_n for the runs. “All GPS” is NRMS of all the GPS velocity residuals. “Profile GPS” is NRMS of GPS velocity residuals for sites within 20 km of the Profile line shown in Figure 12d. “INYO GPS” is NRMS of GPS velocity residuals for sites within the INYO block. “Fault slip rate” is NRMS of all fault slip rates, and “Slip vectors” is NRMS of all earthquake slip vectors. Most data are fit better at slip rates of 5 to 6 mm/yr. (b and c) Profiles along the line shown in Figure 12d. Solid lines are calculated curves. In Figure 12b, no permanent strain rates are allowed in blocks; dashed lines show block motions. In Figure 12c, permanent strain rates are estimated for INYO and PANA blocks; dashed lines show combination of block motions and permanent strain rates. (d) Map of ECSZ in format of Figures 3a and 3b. Opposing arrows show strain rates in INYO and PANA blocks. Gray vectors show residual GPS velocities with 70% confidence ellipses. Including strain within the blocks decreases the estimate of the AL slip rate from 5.9 mm/yr (Figure 3a) to 4.3 mm/yr.

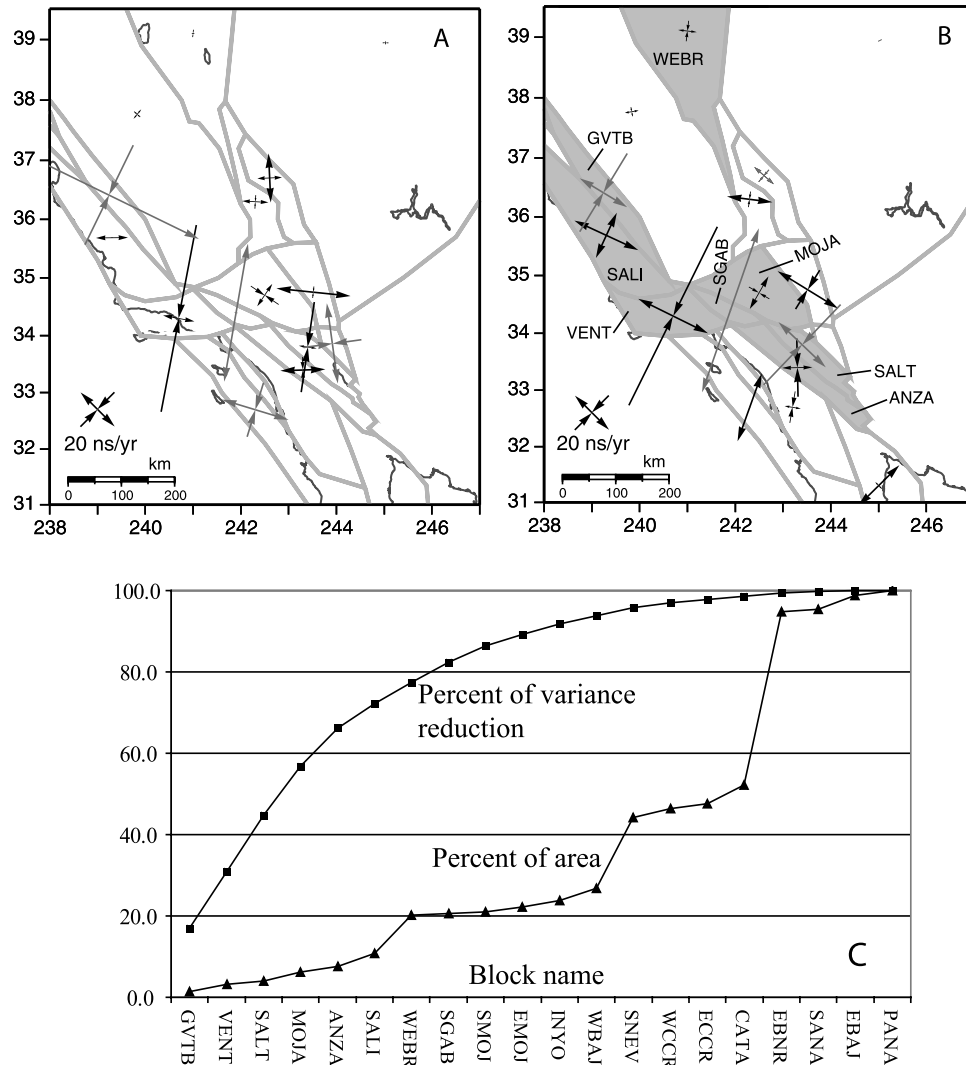


Figure 13. Estimated principal strain rates in blocks exclusive of elastic strains. (a) Strain rates estimated from velocity residuals of elastic block inversion. (b) Strain rates estimated by simultaneous inversion for strain rates along with block rotations and elastic strain. For both Figures 13a and 13b, black arrows indicate those with formal uncertainties less than 10 nanostrain/yr, gray are those with uncertainties between 10 and 20 nanostrain/yr, and those with uncertainties greater than 20 nanostrain/yr are excluded. (c) Cumulative plot of the variance reduction produced by allowing permanent strain rates within each block individually. Blocks are aligned along the horizontal axis in order of decreasing variance reduction. Also shown is the cumulative percent of block area. This shows that a large fraction of the variance reduction by allowing permanent strain rates in the blocks comes from a relatively small area.

variance reduction cover only about 20% of the area (Figures 13b and 13c). Some of the blocks with significant permanent strain rates (GVTB, VENT, SALT, ANZA and SALI) show orientations of the strain rates consistent with right-lateral shear on NW trending planes (Figure 13b). It is possible that some of this strain is unmodeled elastic strain arising from incorrect block or fault geometry. If this is the case, then 20% is an overestimate of the region of permanent distributed strain rates. In either case, the modern strain rates that are not directly related to faults bounding large

blocks appear also to be localized rather than distributed over the western United States.

5. Block Motions

[50] The angular velocities of the blocks in general indicate clockwise (looking from above) rotation around poles to their northeast. Projections of the angular velocities onto the Earth's surface fall between the western United

States and the Pacific–North America pole (Figure 7b) apparently close to the great circle path connecting them. The blocks do not rotate about the PACI-NOAM pole yet are apparently influenced in some way by that motion. The SMOJ, EBNR, and MOJA (off the map to the west) blocks have their poles to the west but with anticlockwise rotation which is consistent with the NW direction of PACI-NOAM motion but not its sense of rotation. The uncertainties in the blocks' angular velocities are elongated to the northeast due to the small NE dimensions of the blocks. However the NW-SE positions are relatively well constrained because the GPS velocities are close in azimuth to the PACI-NOAM velocities. The rotations of most of the blocks are discussed below and the following presents some regional details of interest.

5.1. Eastern Basin and Range

[51] The EBNR block is here defined as the region from the Wasatch front in the east to the ECSZ and Fairview Peak region (242° E) in the west. GPS results of *Thatcher et al.* [1999] demonstrate that the eastern Basin and Range exhibits low strain rates. Within this block, 160 GPS vectors indicate an anticlockwise rotation relative to NOAM about a pole offshore northern Baja (Figure 7b). This rotation produces extension at 4.0 ± 0.2 mm/yr across the Wasatch front near Salt Lake and 2.3 ± 0.2 mm/yr in NW Arizona. Principal strain rates within the EBNR block are also small (<2 ns/yr) (Figure 13). GPS velocities east of the ECSZ [McCluskey et al., 2001] are consistent with being on this rotating block (Figures 1 and 2).

5.2. Western Basin and Range

[52] As noted by others, the modern deformation in the Basin and Range occurs at its westernmost 200 km. This area was included as a separate block bounded by faults. The east and west bounding faults, assumed to dip 60° toward the interior of the block (as done by *Thatcher et al.* [1999]), do not completely explain the strain within the region (Figure 9, line 7). The estimated strain rate tensor within the block is -8 ± 1 ns/yr of nearly north-south (azimuth $-7^{\circ} \pm 5^{\circ}$) contraction and 9 ± 3 ns/yr nearly east-west extension. This tensor indicates right-lateral shear on NW planes, consistent with the extension of the eastern California shear zone into the Walker Lane Belt of northeastern California.

5.3. Sierra Nevada–Great Valley

[53] Several poles of rotation of the Sierra Nevada–Great Valley (SNEV) block have been estimated from geologic and geodetic data [Minster and Jordan, 1987; Argus and Gordon, 1991, 2001; Hearn and Humphreys, 1998; Dixon et al., 2000]. Here I use 86 GPS vectors (NRMS = 1.37, WRMS = 1.1 mm/yr) and slip on bounding faults to estimate a new angular velocity which is northwest of the PACI-NOAM pole (Figure 7b) and about half of the rate. An inversion with the SNEV-NOAM pole fixed to the *Dixon et al.* [2000] vector resulted in an increase in misfit variance with a 6% chance of being random so the new pole is a significant improvement. As noted earlier, the inclusion of strain rate parameters for the SNEV block resulted in a small reduction in the misfit variance and low strain rates suggesting that the SNEV block moves as a rigid entity

once elastic strain is removed. It is notable that elastic strain from the San Andreas fault produces observable perturbations to the velocity field across the entire SNEV block. Hence no point on the SNEV block truly represents its rigid-body motion.

[54] The new pole for the SNEV block indicates that it rotates clockwise relative to NOAM, opposite to the sense of the previous poles (which are all to the SW of the SNEV block) but in the same sense as the PACI-NOAM rotation. However, the vertical axis rotation rate of the SNEV block relative to North America is about $-0.4^{\circ}/\text{Ma}$ (Figure 14), which is less clockwise than that of PACI (about $-0.6^{\circ}/\text{Ma}$). As is discussed below, right-lateral Pacific-North America shear should drive clockwise rotation of the blocks in both the Pacific and North American reference frames. Yet the SNEV block appears to rotate at approximately $0.2^{\circ}/\text{Ma}$ anticlockwise relative to the Pacific suggesting its motion is not entirely due to PACI-NOAM shear. The anticlockwise component could be due to opening in the Basin and Range (extension at the Wasatch front and shear in the western Basin and Range) that pushes the northern half of SNEV westward. Both the EBNR and WEBR blocks rotate anticlockwise relative to the majority of the blocks and PACI (Figure 14b). An alternative explanation for the rotation of SNEV is that the westward motion of the Oregon block [McCaffrey et al., 2000] drags the SNEV block westward at its northern end. However, preliminary results of GPS work in Northern California and southern Oregon [Vollick et al., 2003] suggest that SNEV moves west relative to Oregon, providing the wrong sense of drag. It then appears that the westward motion of the SNEV block may be a reaction to extension in the Basin and Range and not a cause of it, as suggested by *Thatcher et al.* [1999].

6. Vertical Axis Rotations

[55] Rotations of crustal blocks about vertical axes within wide deforming zones are of interest for a number of reasons. Rates of rotation are often used to test among competing models of what drives continental deformation [e.g., McKenzie and Jackson, 1983; Lamb, 1987; Jackson and Molnar, 1990; Schouten et al., 1993]. Spinning blocks can also accommodate some of the relative motion across the deforming region and decrease the amount of faulting necessary [Wallace et al., 2004b]. As noted above, the angular velocities of most of the blocks in the western United States relative to North America appear to fall in a vertical plane that contains the PACI-NOAM angular velocity and the vector pointing at the block from the Earth's center (Figure 7b). In the following I discuss the expected vertical axis rotation rates (called "spin rates" for simplicity) for a deforming zone between plates that rotate relative to one another and compare these to the vertical axis rotations estimated for the western U.S. blocks. Then I discuss the relationship of the spin rates to faulting.

[56] *McKenzie and Jackson* [1983] and *Lamb* [1987] derived expressions for the rotations of blocks floating in a shear zone between two plates in relative motion but not rotating. Following their reasoning I derive the case where one plate rotates relative to the other on a sphere and the

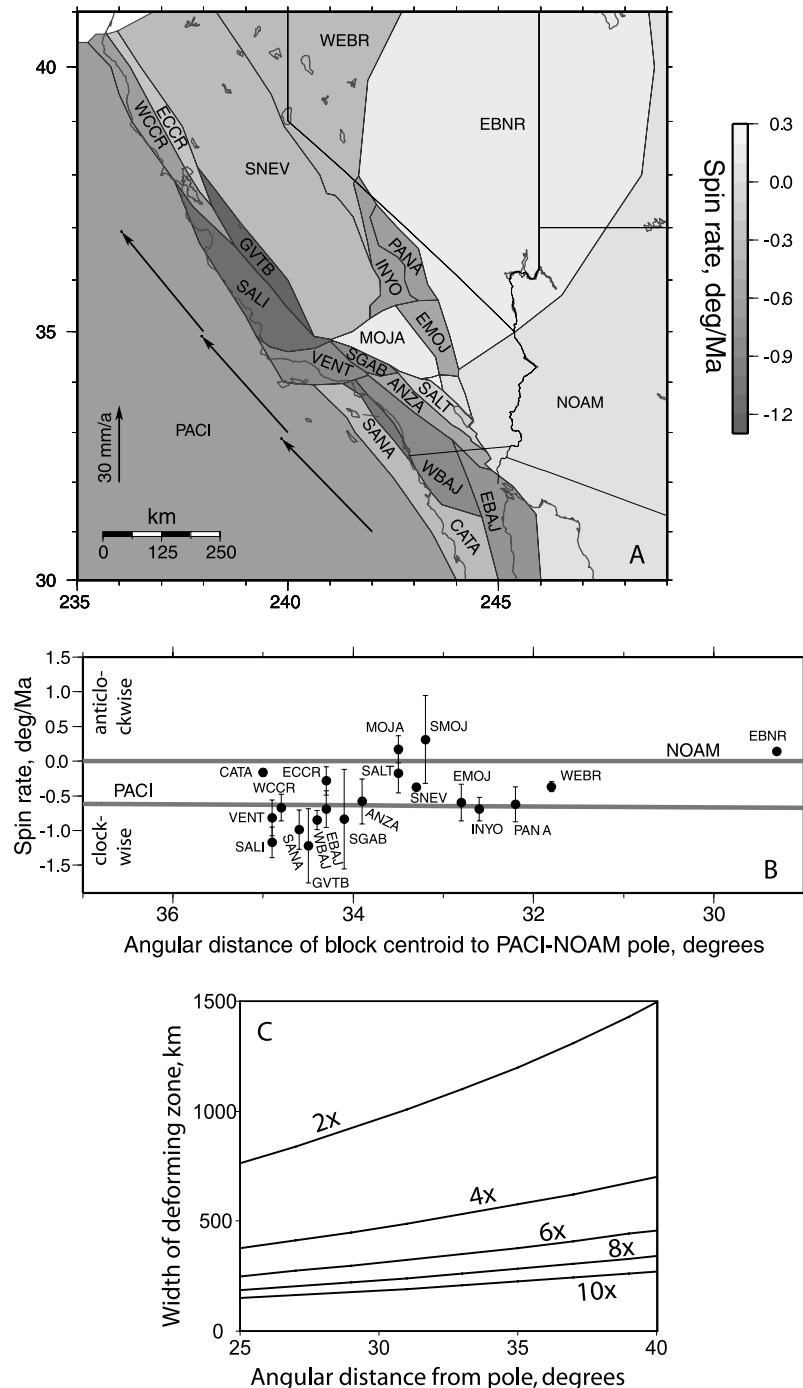


Figure 14. (a) Estimated spin rates (vertical axis rotation rates) for blocks in the western United States relative to North America. (a) Map of blocks showing spin rates with scale at right scale. Negative spin rates represent clockwise as looking from above. (b) Plot of spin rates as distributed with the angular distance of the centroid of the block from the PACI-NOAM pole. Predicted spin rates on the Pacific and North American plates are shown for reference. (c) Expected amplification factor for the spin rate of a block sitting in a shearing substrate as a function of the distance of the shear zone to the relative pole of rotation and the width of the shear zone. See color version of this figure in the HTML.

boundaries of the deforming zone between them forms small circles about the relative rotation axis. Consider plate L rotating with an angular velocity $L\Omega_R$ relative to fixed plate R (Figure 15a). The deforming zone (DZ) between

plates L and R falls between small circles A and B at angular distances Δ_A and Δ_B from $L\Omega_R$. The transverse velocity magnitude of plate L relative to R at a point on the surface of plate L is

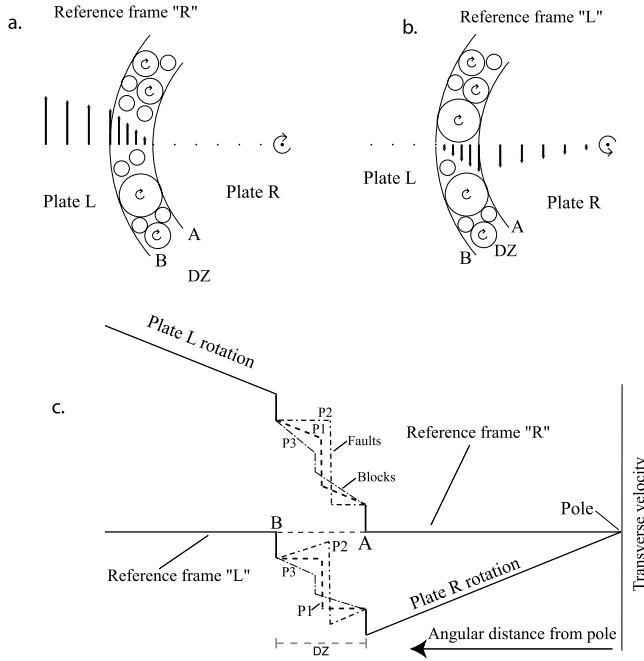


Figure 15. (a and b) Transverse velocities for plates in relative rotational motion and separated by a deforming zone (DZ) bounded at A and B. The two examples in Figures 15a and 15b differ only in which plate is the reference frame. Dot with a spin symbol shows the pole and sense of rotation. (c) Profiles of expected transverse velocities for the two reference frames. When the reference frame is plate R, a higher average gradient in velocity is seen across the DZ. Dashed lines show possible velocity profiles that include block rotations as described in the text.

$$v_0 = |{}_L\Omega_R \times \mathbf{p}| = \omega R_e \sin \Delta, \quad (1)$$

where \mathbf{p} is the vector from the center of the Earth to the surface point, ω is the magnitude of ${}_L\Omega_R$, R_e is the radius of the Earth, Δ is the angle between ${}_L\Omega_R$ and \mathbf{p} , and θ is the direction parallel to the small circle. At the same point the vertical axis rotation rate (ω_r) of plate L; that is, the scalar rate of spin about an axis passing through the surface point and the center of the Earth is

$$\omega_r = {}_L\Omega_R \cdot \mathbf{q} = \omega \cos \Delta, \quad (2)$$

where \mathbf{q} is the unit vector in the direction of \mathbf{p} . The vertical axis rotation rate on a plate increases toward the rotation axis where it reaches a maximum of ω . From (1) the gradient at the surface of the transverse velocity along the great circle containing \mathbf{p} and Ω is

$$dv_0/d\Delta = \omega R_e \cos \Delta. \quad (3)$$

Combining (2) and (3),

$$\omega_r = R_e^{-1} dv_0/d\Delta,$$

indicating that the spin rate for a rigid plate on a sphere is proportional to the transverse velocity gradient (clockwise rotation is negative).

[57] Within the deforming zone, between the small circles A and B, in reference frame R (Figure 15a), the surface velocity v_0 changes from $\omega R_e \sin \Delta_B$ at Δ_B to 0 at Δ_A . The average transverse velocity gradient within this zone due to the relative motion of the bounding plates is then

$$dv_0/d\Delta = (\omega R_e \sin \Delta_B)/(\Delta_B - \Delta_A). \quad (4)$$

[58] Part of this total velocity gradient across the deforming zone is due to rigid body rotation and part is due to the shear between the bounding plates. The average rigid body rotation contribution is

$$\omega R_e (\sin \Delta_B - \sin \Delta_A)/(\Delta_B - \Delta_A), \quad (5)$$

and the shearing component to drive the “excess” block rotations is

$$\omega R_e \sin \Delta_A/(\Delta_B - \Delta_A). \quad (6)$$

According to the floating block concept, a circular block embedded in the shearing basal fluid will rotate at one half the vorticity of the fluid [McKenzie and Jackson, 1983; Lamb, 1987] so we might expect an excess rotation of blocks within the deforming zone at a rate of

$$0.5 \omega R_e \sin \Delta_A/(\Delta_B - \Delta_A). \quad (7)$$

Alternatively, if the blocks are driven by frictional contact with the edges on the deforming zone or other blocks (the “pinned block” or “ball-bearing” model), the excess rotation rate is expected to be equal to (6) [Beck, 1976; Schouten et al., 1993]. The excess rotation rates given by either (6) or (7) can be many times larger than the rigid body component (5).

[59] In the North America reference frame, the vertical axis rotation rate of the Pacific plate (PACI) extended into California is about $-0.6^\circ/\text{Ma}$ (solid line labeled PACI in Figure 14b; negative rotation rates are clockwise looking from above) and is zero for the NOAM plate. The spin rates (ω_r) for many blocks calculated from their angular velocities using (2) are indistinguishable from that of the PACI. Three blocks seem to rotate clockwise faster than PACI (SALI, SANA and GVTB) and only the eastern Basin and Range (EBNR) block rotates anticlockwise significantly relative to North America (NOAM). The remaining blocks fall between the Pacific and North American spin rates (Figure 14b).

[60] As noted above, if blocks within a deforming zone are relatively free to spin in response to the shear of the fluid below, they will spin at least as rapidly as the relative plate spin rate. The expected amplification of the block’s spin rate relative to the plate spin rate can be estimated by taking the ratio of (7) to (5). If f is the spin rate amplification factor, then the width of the deforming zone needed to produce an amplification of f (for the floating block case) is

$$\Delta_B - \Delta_A = \sin^{-1} [(2f)^{-1} (2f + 1) \sin \Delta_A] - \Delta_A. \quad (8)$$

According to (8), at the distance of California from the Pacific–North America rotation axis ($\Delta_A = 30^\circ$ to 35°),

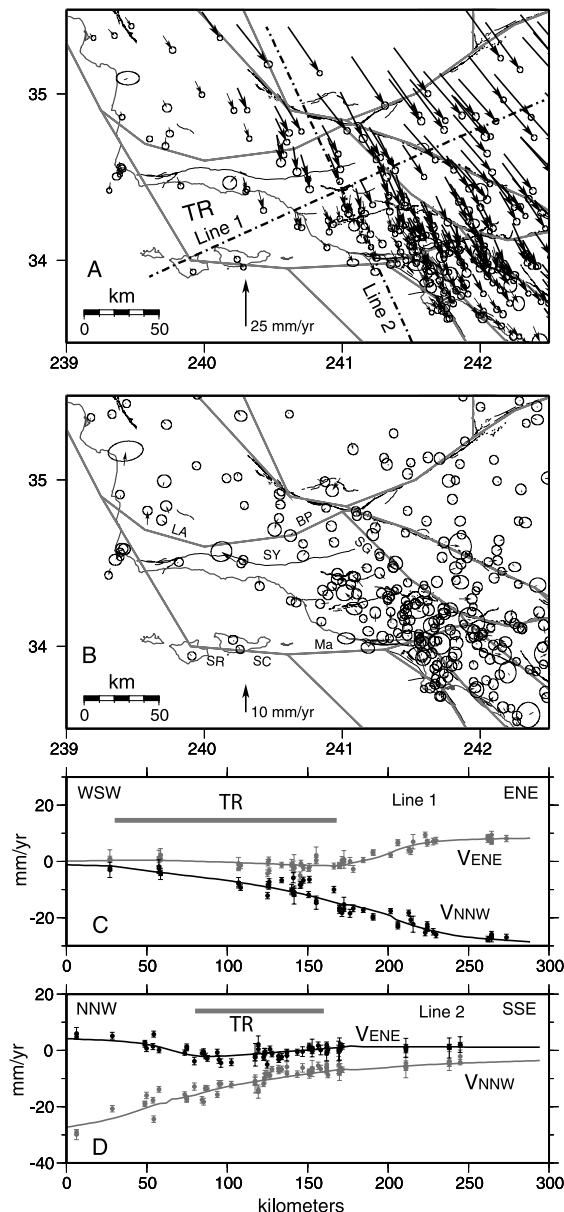


Figure 16. (a) GPS velocities from the Transverse Ranges (TR) region in Pacific plate reference frame. Dashed lines show profile line locations in Figures 16c and 16d. (b) GPS velocity residuals from the area of the Transverse Ranges for the model in which the TR (block VENT) rotates at about the same rate as the Pacific. Faults are indicated by Ma, Malibu coast fault; SR, Santa Rosa Island fault; SC, Santa Cruz Island fault; SG, San Gabriel; SY, Santa Ynez; BP, Big Pine; LA, Los Alamos fault. (c and d) Profiles of GPS velocities across TR. Line 1 points to the ENE, and line 2 points to the SSE. Gray dots (observed GPS) and lines (calculated velocities) show component of velocity along the profile direction (positive is ENE for line 1 and NNW for line 2). Black dots and lines show velocity component normal to profile directions (positive is NNW for line 1 and ENE for line 2). Gray bars show where the profile lines cross the TR; the lack of an obvious, unmodeled gradient in the profile-normal (black) velocities across the TR suggests that rapid rotation of the TR does not occur today.

equidimensional blocks within a shear zone 1000 km wide would rotate twice as fast as the Pacific (Figure 14c). They would rotate 4 times faster in a 500 km wide zone, and 6 to 10 times faster in a 200 to 300 km wide zone. The estimated spin rates for the western U.S. blocks are at most twice the Pacific rate (Figure 14b). In the context of the foregoing assumptions, the vertical axis rotations of the blocks suggest a very wide shear zone if the blocks are driven by basal shear. If the blocks are driven by edge tractions in the manner of ball bearings, their spin rates would be twice as fast as the floating block case for a given shearing gradient, making this an even more unlikely mechanism.

[61] The spins of blocks overlying mantle shear zones can vary due to blocks' shapes and their interactions across block-bounding faults [Lamb, 1994a]. Blocks that are elongated along the direction of shearing will rotate little since the underlying fluid does not exert torque on them. Hence the observed subdued spin rates may be due to the elongated shapes of the blocks parallel to the Pacific–North America shear zone indicating little about the basal shear [Lamb, 1994b]. One clear exception to the tendency of the blocks to be elongated along strike is the Transverse Ranges block (VENT), which is discussed next.

6.1. Transverse Ranges

[62] The Transverse Ranges have been the focus of attempts to tie rotations to driving mechanisms due to their oblique orientation relative to plate motion and because paleomagnetic declination anomalies indicate large clockwise rotations in the past [Luyendyk *et al.*, 1980; Luyendyk, 1991]. Jackson and Molnar [1990] and Molnar and Gipson [1994] summarize paleomagnetic evidence for rapid ($5^{\circ}/\text{Ma}$ clockwise) rotations of the crust within the Transverse Ranges. They suggest that modern VLBI data are consistent with such rates, indicating that the rotations continue. Donnellan *et al.* [1993] also infer rapid rotation rates from small subsets of geodetic sites whose velocities are estimated from early GPS (1987 to 1992). Lamb [1994b], however, predicts rotation rates at about half the paleomagnetic rate from inversions of kinematic data. I did not attempt to model in detail the deformation within the Transverse Ranges because the faults are closely spaced and it is unlikely that the geodetic data can resolve the distribution of slip among them. The northern and southern boundaries for the block (VENT) containing Transverse Ranges (TR) are chosen to fall along the northern and southern extremes of the easterly trending faults (Big Pine fault in north and Malibu Coast fault in south; Figure 16b).

[63] The inversion results in a large-scale spin rate of the VENT block of $-0.8 \pm 0.3^{\circ}/\text{Ma}$, which is only slightly faster clockwise than the expected spin rate of the Pacific plate at this point. The block inversion matches most of the GPS vectors within the block (Figure 16) and earthquake slip vectors near the edges of the block (Figure 3b). A $5^{\circ}/\text{Ma}$ rotation rate is approximately equivalent to a velocity gradient of 80 nrad/yr; that is, a change of 8 mm/yr over 100 km distance. The velocity residuals do not show a systematic pattern that would indicate blocks rotating at this rate (Figures 16b–16d). An inversion in which a faster spin rate of $-1.2^{\circ}/\text{Ma}$ was imposed on VENT resulted in doubling the misfit variance of the GPS velocities within the block, indicating that the elastic strain rates from nearby

faults do not appreciably trade off with block rotation. Finally, the GPS velocities do not show the gradients that indicate rotation; while there is a gradient in the NNW component along ENE trending line 1, no corresponding gradient in the ENE component along NNW trending line 2 is evident (Figures 16c and 16d). Hence the rapid vertical axis rotation rate in the Transverse Ranges evident in paleomagnetic data does not seem to be continuing today.

6.2. Rotations and Fault Slip Rates

[64] Kinematically, rotations and faulting are related in that spinning blocks can take up some part of the velocity gradients within a deforming zone and reduce the amount of faulting required. For example, the oblique convergence of the Pacific plate with Australia across North Island, New Zealand, is fully partitioned yet only one third of the margin-parallel slip is taken up on crustal strike-slip faults [Wallace *et al.*, 2004b]. The remaining motion occurs by crustal block rotations.

[65] In contrast, I suggest here that in the western United States nearly all of the motion of North America relative to the Pacific across the deforming zone (DZ) is taken up by faulting while Pacific relative to North America motion is accommodated by a combination of block rotation and faulting. This apparent paradox arises because the relative velocities between the two plates changes across the width of the deforming zone as the distance to the rotation axis changes; that is, points on the Pacific at the western edge of the DZ moves faster relative to North America than do points on the North America plate at the eastern edge of the DZ relative to the Pacific (because the pole is to the east).

[66] The analysis above was done in the reference frame of plate R, on the same side of the deforming zone (DZ) as the rotation pole (Figure 15a), analogous to using North America as the reference frame for western U.S. deformation. However, if one uses plate L as the reference frame, the velocity gradient across the deforming zone is apparently smaller (Figures 15b and 15c). The difference in the estimated gradients is due to the velocity gradient across the DZ arising from the relative rotation of the bounding plates (5). The edge of the DZ on plate L moves at a rate $\omega_e \sin \Delta_B$ relative to plate R, while the edge of the DZ on plate R moves at $\omega R_e \sin \Delta_A$ relative to plate L. The two rates differ by $\omega R_e (\sin \Delta_B - \sin \Delta_A)$ so the average gradient is given by (5). Clearly this difference in gradients arises from fixing one side of the DZ or the other at zero velocity when the two edges of the DZ do not have the same velocities in their respective reference frames. For the western United States, the velocity difference in the two reference frames is close to 5 mm/yr (calculated between 35°N, 245°E and 33°N, 241°E).

[67] Unlike rotations, fault slip rates are invariant to the choice of reference frame. If one goes from west to east across the western United States adding up fault slip rates the same total should be obtained by going from east to west [Humphreys and Weldon, 1994]. However, as shown above, the total expected slip rate (assuming faulting only) will change depending on the assumed reference frame. In the Pacific reference frame, faulting alone may account for North American motion while in the North American reference frame faulting alone cannot account fully for Pacific motion.

[68] To show this graphically, Figure 15c shows hypothetical velocity profiles across the deforming zone in both reference frames (RFs). In reference frame R there is more total slip required across the deforming zone (DZ) than in reference frame L. The lines labeled P1 (in both RFs) are for the case in which the blocks spin in RF R at the same rate as plate L but do not rotate in RF L (faults are shown by vertical lines; block rotations by sloping line segments between faults). In both RFs the total faulting (the sum of the steps in velocity profiles) is the same. In profile P2, in which the blocks do not rotate in RF R, they must rotate in the same sense (anticlockwise in the example shown) as plate R in RF L to keep the amount of faulting the same in both RFs. However, the anticlockwise rotation of the blocks is opposite the sense of shear across the deforming zone (Figure 15b) and is not likely to occur if the deformation is driven by plate edge stress or basal tractions alone. The profile P3 shows the case in which the blocks rotate clockwise in RF R faster than plate L and therefore also rotate clockwise relative to plate L, consistent with the sense of shear in both reference frames. In this case, the amount of faulting necessary is reduced further. Therefore this suggests that if the block motions are driven by the relative motion of the plates bounding the DZ, the maximum total faulting (i.e., profile P1) across the DZ is given by the relative motion in reference frame L, which will be less than the amount of total slip in RF R. Moreover, if the blocks within the DZ spin clockwise at a rate less than that of plate L, then they are spinning anticlockwise relative to plate R.

[69] For the Pacific–North America boundary, this has two implications. First, blocks that are rotating in response to the plate boundary shear (edge or basal) should spin clockwise at least as fast as the Pacific (in the NOAM frame). Those that rotate more slowly (i.e., with spin rates more positive than the PACI spin rate; Figure 14b) are rotating anticlockwise relative to the Pacific, opposite the sense of PACI-NOAM shear (PACI-NOAM shear is right-lateral leading to clockwise block rotations in either RF; see Figures 15a and 15b), and are likely responding to other forces. The northern half of the region, including the EBNR, WEBR, SNEV, and ECCR blocks are rotating anticlockwise relative to the Pacific (Figure 14). Collapse of the Colorado Plateau [e.g., Jones *et al.*, 1996] may be driving the northern EBNR westward which in turns applies an anticlockwise component to the WEBR and SNEV blocks that would otherwise spin clockwise at nearly the rate as the Pacific. Blocks that spin faster clockwise (more negative spin rates) than the Pacific may be driven to some extent by basal or edge tractions, although only one block (SALI) seems to rotate clockwise significantly relative to PACI (Figure 14b).

[70] Second, in the summing of fault slip rates along profiles across the deforming zone it should be recognized that block rotations play different roles in the two reference frames. In the North America reference frame the overall rotation of the western United States must be taken into account as it can add a significant amount (10% or more) to the velocity gradient (Figure 15c). Humphreys and Weldon's [1994] path integrations from east to west in the NOAM reference frame, in my opinion, underestimated the role of

rotations, and considering that they obtained a good agreement with Pacific–North America motion (48 mm/yr offshore California), I would argue that they overestimated the total faulting (except for their southernmost path, which includes significant rotations).

6.3. Why Blocks Do Not Rotate About Pacific–North America Pole

[71] The foregoing argument that blocks driven by shear forces within the deforming zone spin clockwise at least as fast as the Pacific plate can explain why the blocks, even if driven by Pacific–North America shear, do not rotate about an angular velocity parallel to that of Pacific–North America. All blocks within the deforming zone move more slowly to the northwest relative to North America than does the Pacific, revealed by the step-like decrease in block velocities toward North America in the NE trending profiles (Figure 9). For a block at an angular distance Δ from its angular velocity, its transverse velocity is $v_\theta = \omega R_e \sin \Delta$. Hence the easterly decreasing velocities could be satisfied if the blocks rotate, relative to North America, about the same pole as the Pacific (Δ approximately equal for all blocks) but at easterly decreasing rates (i.e., changes in ω largely control the velocity variations). However, in this case the blocks' spin rates, $\omega_r = \omega \cos \Delta$, would also decrease rapidly eastward. The eastern blocks would then be spinning anticlockwise relative to the Pacific, opposite the sense of shear of the Pacific–North America motion. (Both $\sin \Delta$ and $\cos \Delta$, relative to the PACI-NOAM pole location, vary by less than 10% over the width of the western United States deforming zone so these terms do not contribute much to the velocity and spin gradients.) Instead, the near constancy of the spin rates ($\omega \cos \Delta$) suggests instead that as ω decreases eastward, Δ also decreases while the velocity ($\omega R_e \sin \Delta$) decreases. The decrease in Δ means that as the block slows, its angular velocity (pole of rotation) moves closer to it.

7. Discussion

[72] The short-term geodetic surface velocity field alone in the western United States or elsewhere contains little information about the rheology of the deforming material. Accordingly, a variety of types of models that have different rheological underpinnings can fit the observations satisfactorily but do not necessarily support the uniqueness of such a rheology. Hence it remains debated whether the deformation within continents is more due to a viscous behavior of the lower crust and upper mantle or to plate-like behavior of the lithosphere.

[73] Arguments are couched in terms of the degree to which the long-term deformation of the Earth's surface is continuous or discontinuous [Thatcher, 2003]. In the continuum concept, even though the upper brittle layer of the Earth is clearly broken into faults, the faults are thought to be relatively closely spaced, have small slip rates and extend only into the lower crust. Even though locally the surface deformation may be different than that in the substrate below, the idea is that the average velocity mimics that of the viscous substrate [Bourne *et al.*, 1998]. In the plate (block) model, which is similar to plate tectonics, the faults can be widely spaced, rapidly slipping, and extend vertically

through the entire lithosphere (though not as velocity discontinuities).

[74] In most regions the decade-scale surface velocity field is continuous and observed strain rates can be matched either by coupling of the thin surface layer with a continuously deforming viscous substrate or by elastic strain arising from crustal blocks being stuck together at faults. If one had reliable long-term slip rates on all crustal faults we could solve the problem directly. However, fault slip rate data are incomplete and we therefore often rely on short-term geodetic data to estimate long-term slip rates on faults, with mixed results. The approach I have taken is to combine the geodetic and geologic data so that the predicted elastic strains computed near faults are consistent with what is known about the slip rates on the faults. Moreover, the calculated fault slip rates, because they are computed from a finite number of angular velocities of blocks, satisfy the kinematic boundary condition imposed by Pacific–North America relative motion.

[75] Most of the strain rates observed within the deforming region of the southwest United States can be explained as the elastic response to stuck faults; that is, they are associated spatially with known faults and are consistent with the slip rates and senses of slip on those faults. In general, the largest strain rates are associated with the fastest faults. In the continuum view, surface strain rates should be smoothly varying and there is little reason that they should be localized at faults or be correlated with the surface faults. Nevertheless, studies like that of Flesch *et al.* [2000], in which lithospheric viscosity is derived from surface strain rates and gravitationally driven stress, suggest that faults are regions of low viscosity, probably because there is no mechanism for increasing the stress near surface faults in such models. In the end, the inferred viscosity distribution looks similar to the strain rate distribution and inferred stress variations play a minor role.

[76] As Thatcher *et al.* [1999] suggest, a strong argument against the continuum model is the lack of obvious geodetic deformation within the 800 km wide eastern Basin and Range (EBNR). In my inversion, the EBNR has 160 GPS vectors that are fit as a rotating block with residual NRMS = 1.02 and WRMS = 0.9 mm/a (Table 1) and an average uniform strain rate of <3 nanostrain/yr. Strain rates within the EBNR based on gravitational arguments are expected to be high [Flesch *et al.*, 2000] and the lack of deformation has led to inferences of a high viscosity for it. The second largest block is the Sierra Nevada (SNEV) block. After correcting for elastic strain, largely from the San Andreas, the SNEV block is also nearly rigid (residual average strain rate <3 nanostrain/yr).

[77] It is rather surprising to find that block spin rates in the western United States are subdued relative to other parts of the world. We have shown in other regions, such as Papua New Guinea [Wallace *et al.*, 2004a], New Zealand [Wallace *et al.*, 2004b], and elsewhere [McCaffrey and Wallace, 2004], by comparisons with paleomagnetic rotation rates, that the block inversion method using GPS velocity fields can detect rapid rotations even in the presence of large fault-induced strain rates. One possibility for the lack of rotation in the western United States is that the blocks are elongated in the direction of shear and hence are stable [Lamb, 1987]. However, the Transverse Ranges,

which are highly oblique to the shear direction, also do not show evidence of rapid rotations in recent geodetic data.

[78] Another possibility for the low rotation rates is that the rates of faulting modulate the rotations. In the western United States, the fault slip rates are close to the maximum expected and block rotations take up very little of the deformation (for example, profile P1 of Figure 15c). In contrast, Wallace *et al.* [2004b] show that in North Island, New Zealand, faulting appears to accommodate only one third of the shear component while block rotation takes up the other two thirds. Wallace *et al.* [2004c] attribute the rapid rotations at subduction zones such as New Zealand to collisions of buoyant features on the downgoing plate with the subduction zone.

[79] Lamb [1994a] examined the relative magnitudes of edge forces (faults) and basal traction in applying vertical torque to crustal blocks. For roughly equidimensional blocks the ratio of basal to edge torque is proportional to

$$l \eta \varepsilon / h \tau, \quad (9)$$

where l is the characteristic block dimension, η is the viscosity of the substrate, ε is the basal strain rate, h is the block thickness, and τ is the fault shear stress. He concluded that the ratio of the basal-derived torque to edge-derived torque could range from 0.01 to 1000 depending on reasonable ranges of values for pertinent parameters. Therefore either mechanism can act in nature.

[80] Here I argue that a large part of the southwestern U.S. deformation is driven by forces acting across the edges of the blocks. The primary evidence for this is the near constancy of the vertical axis rotation rates of the blocks and that this rate is similar to that of the relative rotation rate of the bounding Pacific and North American blocks. The spin rates of the blocks can be controlled either by basal shear or edge tractions. As shown earlier, basal shearing should cause the rotations to be considerably faster than observed unless the shear zone is on the order of 1000 km wide (Figure 14c). While many of the blocks are elongated, some do not have their long axes parallel to PACI-NOAM shear and therefore should show more rapid rotations [Lamb, 1987] or at least a less ordered pattern of rotations.

[81] If we think of faults as resisting block rotations, rather than driving them, then a low ratio in equation (9) is consistent with low rotation rates and relatively strong faults. Figure 15 and the accompanying discussion suggest that there is a kinematic trade-off between rates of rotation and faulting such that the velocity gradients they produce have to sum to the total transverse slip rate across the deforming region [Lamb, 1994a]. If the faults are oriented such that they can slip easily in the direction of shear, then rotations are kinematically and mechanically less likely to contribute to the shear deformation.

[82] Finally, the constancy of the blocks' spin rates suggests that the blocks are in mechanical contact along significant sections of their boundaries. The spin rates are characterized by velocity gradients that are apparently communicated from block to block. Transmitting a spin rate from one rigid block to another requires a long common boundary (how long is unknown). If their contact areas were

limited in extent, their rotation rates would probably be enhanced by the ball-bearing effect which does not appear to be occurring.

8. Conclusions

[83] Geodetic, geologic, and seismological data are inverted for angular velocities of and strain rates within a finite number of lithospheric blocks representing the southwestern United States. The results indicate that to a large degree the region can be represented with a plate-tectonic style of deformation and relatively minor regions of small-scale deformation. The similarities of the vertical axis rotation rates of the blocks to each other and to the Pacific plate, relative to North America, suggest that western U.S. deformation is in large part a response to edge-driven Pacific–North America shear. Some areas rotate anticlockwise relative to the Pacific, opposite to the sense of shear, and are likely responding to other forces, such as gravitational collapse of the elevated continental interior.

Appendix A

[84] To scale uncertainties in the GPS velocity fields, I first looked at the distribution of the quantity

$$(V_{F1} - V_{F2})/\sigma_{F1},$$

where $F1$ and $F2$ are the two velocity fields being compared, and V and σ are the velocity (for east or north) and the standard deviation, respectively. This quantity is calculated for each common site and the standard deviations are estimated for east and north independently. Using the 185 common sites of the WUSC [Bennett *et al.*, 1999] and CMM3 velocity fields, the standard deviations in the velocity differences normalized by the WUSC uncertainties is 6.8 for the east component and 5.9 for the north component. Using the CMM3 uncertainties instead of the WUSC to normalize the velocity differences results in standard deviations of 2.2 and 1.6 for the east and north, respectively, indicating that the larger CMM3 uncertainties represent better the scatter in the velocity differences. A comparison of 115 common velocities of the WUSC and RB03 [Bennett *et al.*, 2003] fields reveals east and north standard deviations of 4.0 and 2.8 when normalized by the WUSC uncertainties, and 5.9 and 5.3 when normalized by RB03 uncertainties. Since the RB03 field is newer than WUSC, the large standard deviations in the normalized differences indicate that the velocity estimate changes were well outside the velocity uncertainties originally assigned to WUSC. An increase by a factor of 2.5 in the WUSC uncertainties brings them into the range expected by this comparison. The RB03 velocity field has 15 sites in common with CMM3; the velocity differences normalized by RB03 uncertainties give north and east standard deviations of 5.7 and 9.4. These are reduced to 0.8 and 1.2 when normalized by the CMM3 uncertainties, suggesting that the RB03 uncertainties are underestimated. Finally, the factor of 2.5 reduces the NRMS of the final model fits to

the WUSC and RB03 velocity fields from 4.53 and 6.90 (original, published uncertainties) to 1.01 and 1.24 (rescaled uncertainties), respectively.

Appendix B

[85] The best fit parameters are those that minimize the reduced χ^2 statistic

$$\chi_n^2 = \left[(N - P)^{-1} \sum_{i=1}^N p_i \right]^{1/2},$$

where N is the number of observations, P is the number of free parameters ($N - P$ is the number of degrees of freedom), and p is a misfit penalty function.

[86] For a single GPS velocity with east and north components V_e and V_n ,

$$p = \mathbf{R}^T \mathbf{C}^{-1} \mathbf{R},$$

where \mathbf{R} is the matrix (R_e, R_n) of velocity residuals, T indicates the transpose of the matrix, and \mathbf{C} is the east-north velocity covariance matrix.

[87] For fault slip rates, when given in terms of a mean rate V and standard error s , $p = R^2/s^2$ where R is the residual. When given as minimum and maximum slip rate values, the residual R is the amount that the calculated value falls outside the measured range. The effective standard error s is taken as one half the range (with a minimum of 1.0 mm/yr). For given minimum and maximum slip rates of V_{\min} and V_{\max} , and a calculated rate of V_c ,

$$p = 0, \quad V_{\min} \leq V_c \leq V_{\max},$$

$$p = [(V_c - V_{\min})/s]^2, \quad V_c \leq V_{\min},$$

$$p = [(V_c - V_{\max})/s]^2, \quad V_c \geq V_{\max},$$

where

$$s = (V_{\max} - V_{\min})/2.$$

In some cases, slip rates are measured in a particular azimuth.

[88] Angular data, earthquake slip vector and transform azimuths, are handled in the manner described by DeMets *et al.* [1990]:

$$p = [2 \sin(R/2)/s]^2,$$

where R and s , the angular residual and standard error, are both in radians.

[89] **Acknowledgments.** Discussions with Bob King, Laura Wallace, Mark Stirling, and Peter Molnar and reviews by Geoff King, Wayne Thatcher, and Don Forsyth are greatly appreciated. Much of this work was done while the author was a guest of the Institute of Geological and Nuclear Sciences of New Zealand, thanks to Laura Wallace, Des Darby, John Beavan, and Hugh Cowan. Figures were made with Generic Mapping Tools software [Wessel and Smith, 1998].

References

- Argus, D. F., and R. G. Gordon (1991), Current Sierra Nevada–North America motion from very long baseline interferometry: Implications for the kinematics of the western United States, *Geology*, **19**, 1085–1088.
- Argus, D. F., and R. G. Gordon (2001), Present tectonic motion across the Coast Ranges and San Andreas fault system in California, *Geol. Soc. Am. Bull.*, **113**, 1580–1592.
- Beanland, S., and M. M. Clark (1994), The Owens Valley fault zone, eastern California, and surface faulting associated with the 1872 earthquake, *U.S. Geol. Surv. Bull.*, **1982**, 29 pp.
- Beavan, J., P. Tregoning, M. Bevis, T. Kato, and C. Meertens (2002), Motion and rigidity of the Pacific plate and implications for plate boundary deformation, *J. Geophys. Res.*, **107**(B10), 2261, doi:10.1029/2001JB000282.
- Beck, M. E. (1976), Discordant paleomagnetic pole positions as evidence of regional shear in the western Cordillera of North America, *Am. J. Sci.*, **276**, 694–712.
- Bennett, R. A., J. L. Davis, and B. P. Wernicke (1999), The present-day pattern of western U.S. Cordillera deformation, *Geology*, **27**, 371–374.
- Bennett, R. A., B. P. Wernicke, N. A. Niemi, A. M. Friedrich, and J. L. Davis (2003), Contemporary strain rates in the northern Basin and Range province from GPS data, *Tectonics*, **22**(2), 1008, doi:10.1029/2001TC001355.
- Boucher, C., Z. Altamimi, P. Sillard, and M. Feissel-Vernier (2004), The ITRF2000, *IERS Tech. Note 31*, 289 pp., Verlag des Bundesamts für Kartogr. und Geod., Frankfurt-am-Main, Germany.
- Bourne, S. J., P. C. England, and B. Parsons (1998), The motion of crustal blocks driven by flow of the lower lithosphere and implications for slip rates of continental strike-slip faults, *Nature*, **391**, 655–659.
- Castillo, D. A., and W. L. Ellsworth (1993), Seismotectonics of the San Andreas fault system between Point Arena and Cape Mendocino in northern California: Implications for the development and evolution of a young transform, *J. Geophys. Res.*, **98**, 6543–6560.
- DeMets, C. (1995), A reappraisal of seafloor spreading lineations in the Gulf of California: Implications for the transfer of Baja California to the Pacific plate and estimates of Pacific–North America motion, *Geophys. Res. Lett.*, **22**, 3545–3548.
- DeMets, C., and T. H. Dixon (1999), New kinematic models for Pacific–North America motion from 3 Ma to present: 1. Evidence for steady motion and biases in the NUVEL-1A model, *Geophys. Res. Lett.*, **26**, 1921–1924.
- DeMets, C., R. G. Gordon, D. F. Argus, and S. Stein (1990), Current plate motions, *Geophys. J. Int.*, **101**, 425–478.
- DeMets, C., R. G. Gordon, D. F. Argus, and S. Stein (1994), Effects of recent revisions to the geomagnetic reversal time scale on estimates of current plate motions, *Geophys. Res. Lett.*, **21**, 2191–2194.
- Deng, J. S., and L. R. Sykes (1997), Evolution of the stress field in southern California and triggering of moderate-size earthquakes: A 200-year perspective, *J. Geophys. Res.*, **102**, 9859–9886.
- Dixon, T. H., M. Miller, F. Farina, H. Wang, and D. Johnson (2000), Present-day motion of the Sierra Nevada block and some tectonic implications for the Basin and Range province, North America Cordillera, *Tectonics*, **19**, 1–24.
- Dixon, T. H., et al. (2002), Seismic cycle and rheological effects on estimation of present-day slip rates for the Agua Blanca and San Miguel-Vallecitos faults, northern Baja California, Mexico, *J. Geophys. Res.*, **107**(B10), 2226, doi:10.1029/2000JB000099.
- Dixon, T. H., E. Norabuena, and L. Hotaling (2003), Paleoseismology and Global Positioning System: Earthquake-cycle effects and geodetic versus geologic fault slip rates in the eastern California shear zone, *Geology*, **31**, 55–58.
- Dokka, R. K., and C. J. Travis (1990), Late Cenozoic strike-slip faulting in the Mojave Desert, California, *Tectonics*, **9**, 311–340.
- Donnellan, A., B. H. Hager, R. W. King, and T. A. Herring (1993), Geodetic measurement of deformation in the Ventura Basin region, southern California, *J. Geophys. Res.*, **98**, 21,727–21,739.
- Dziewonski, A. M., T.-A. Chou, and J. H. Woodhouse (1981), Determination of earthquake source parameters from waveform data for studies of global and regional seismicity, *J. Geophys. Res.*, **86**, 2825–2852.
- Ekström, G., A. M. Dziewonski, N. N. Maternovskaya, and M. Nettles (2005), Global seismicity of 2003: Centroid-moment-tensor solutions for 1087 earthquakes, *Phys. Earth Planet. Inter.*, **148**, 327–351.
- England, P., and D. McKenzie (1982), A thin viscous sheet model for continental deformation, *Geophys. J. R. Astron. Soc.*, **70**, 295–321.
- Flesch, L. M., W. E. Holt, A. J. Haines, and B. Shen-Tu (2000), Dynamics of the Pacific–North American plate boundary in the western United States, *Science*, **287**, 834–836.

- Frankel, A. D., et al. (2002), Documentation for the 2002 update of the national seismic hazard maps, *U.S. Geol. Surv. Open File Rep.*, 02-420.
- Freymueller, J. T., M. H. Murray, P. Segall, and D. Castillo (1999), Kinematics of the Pacific–North America plate boundary zone, northern California, *J. Geophys. Res.*, 104, 7419–7441.
- Hearn, E. H., and E. D. Humphreys (1998), Kinematics of the southern Walker Lane Belt and motion of the Sierra Nevada block, California, *J. Geophys. Res.*, 103, 27,033–27,049.
- Humphreys, E. D., and R. J. Weldon II (1994), Deformation across the western United States: A local estimate of Pacific–North America transform deformation, *J. Geophys. Res.*, 99, 19,975–20,010.
- Jackson, J., and P. Molnar (1990), Active faulting and block rotations in the western Transverse Ranges, California, *J. Geophys. Res.*, 95, 22,073–22,087.
- Jennings, C. W. (1974), Fault activity map of California and adjacent areas with location and ages of recent volcanic eruptions, *Calif. Geol. Data Map Ser.* 6, Calif. Geol. Surv., Sacramento.
- Jones, C. H., J. R. Unruh, and L. J. Sonder (1996), The role of gravitational potential energy in active deformation in the southwestern US, *Nature*, 381, 37–41.
- King, G., D. Oppenheimer, and F. Amelung (1994), Block versus continuum deformation in the western United States, *Earth Planet. Sci. Lett.*, 128, 55–64.
- Lamb, S. H. (1987), A model for tectonic rotations about a vertical axis, *Earth Planet. Sci. Lett.*, 84, 75–86.
- Lamb, S. H. (1994a), Behavior of the brittle crust in wide plate boundary zones, *J. Geophys. Res.*, 99, 4457–4483.
- Lamb, S. H. (1994b), A simple method for estimating the horizontal velocity field in wide zones of deformation—I. Description, with an example from California, *Geophys. J. Int.*, 119, 297–312.
- Lay, T., and S. Schwartz (2004), Comment on “Coupling semantics and science in earthquake research,” *Eos Trans. AGU*, 85, 339–340.
- Luyendyk, B. P. (1991), A model for Neogene crustal rotations, transtension, and transpression in southern California, *Geol. Soc. Am. Bull.*, 103, 1528–1536.
- Luyendyk, B. P., M. J. Kamerling, and R. Terres (1980), Geometrical model for Neogene crustal rotations in southern California, *Geol. Soc. Am. Bull.*, 91, 211–217.
- McCaffrey, R. (2002), Crustal block rotations and plate coupling, in *Plate Boundary Zones, Geodyn. Ser.*, vol. 30, edited by S. Stein and J. Freymueller, pp. 101–122, AGU, Washington, D. C.
- McCaffrey, R., and L. M. Wallace (2004), A comparison of geodetic and paleomagnetic estimates of block rotation rates in deforming zones, *Eos Trans. AGU*, 85, Fall Meet. Suppl., Abstract U32A-08.
- McCaffrey, R., M. Long, C. Goldfinger, P. C. Zwick, J. L. Nabelek, C. K. Johnson, and C. Smith (2000), Rotation and plate locking at the southern Cascadia subduction zone, *Geophys. Res. Lett.*, 27, 3117–3120.
- McCluskey, S., et al. (2001), Present day kinematics of the eastern California shear zone from a geodetically constrained block model, *Geophys. Res. Lett.*, 28, 3369–3372.
- McKenzie, D., and J. Jackson (1983), The relationship between strain rates, crustal thickening, paleomagnetism, finite strain, and fault movements within a deforming zone, *Earth Planet. Sci. Lett.*, 65, 182–202.
- Minster, J. B., and T. H. Jordan (1987), Vector constraints on western U.S. deformation from space geodesy, neotectonics and plate motions, *J. Geophys. Res.*, 92, 4798–4804.
- Minster, J. B., T. H. Jordan, P. Molnar, and E. Haines (1974), Numerical modeling of instantaneous plate tectonics, *Geophys. J. R. Astron. Soc.*, 36, 541–576.
- Molnar, P. (1988), Continental tectonics in the aftermath of plate tectonics, *Nature*, 335, 131–137.
- Molnar, P., and J. H. Gipson (1994), Very long baseline interferometry and active rotations of crustal blocks in the western Transverse Ranges, California, *Geol. Soc. Am. Bull.*, 106, 594–606.
- Morgan, W. J. (1968), Rises, trenches, great faults, and crustal blocks, *J. Geophys. Res.*, 73, 1959–1982.
- Murray, M. H., and P. Segall (2001), Modeling broadscale deformation in northern California and Nevada from plate motions and elastic strain accumulation, *Geophys. Res. Lett.*, 28, 4315–4318.
- Namson, J. S., and T. L. Davis (1988), Seismically active fold and thrust belt in the San Joaquin Valley, central California, *Geol. Soc. Am. Bull.*, 100, 257–273.
- Okada, Y. (1985), Surface deformation due to shear and tensile faults in a half-space, *Bull. Seismol. Soc. Am.*, 75, 1135–1154.
- Peltzer, G., and P. Tapponnier (1988), Formation and evolution of strike-slip faults, rifts, and basins during the India-Asia collision: An experimental approach, *J. Geophys. Res.*, 93, 15,085–15,117.
- Peltzer, G., F. Crampe, S. Hensley, and P. Rosen (2001), Transient strain accumulation and fault interaction in the eastern California shear zone, *Geology*, 29, 975–978.
- Petersen, M. D., and S. G. Wesnousky (1994), Fault slip rates and earthquake histories for active faults in southern California, *Bull. Seismol. Soc. Am.*, 84, 1608–1649.
- Press, W. H., B. P. Flannery, S. A. Teukolsky, and W. T. Vetterling (1989), *Numerical Recipes*, Cambridge Univ. Press, New York.
- Sauber, J., M. Lisowski, and S. Solomon (1989), Geodetic measurement of deformation east of the San Andreas fault in central California, in *Slow Deformation and Transmission of Stress in the Earth, Geophys. Monogr. Ser.*, vol. 49, edited by S. C. Cohen and P. Vanicek, pp. 71–86, AGU, Washington, D. C.
- Savage, J. C. (1983), A dislocation model of strain accumulation and release at a subduction zone, *J. Geophys. Res.*, 88, 4984–4996.
- Savage, J. C., W. Gan, and J. L. Svart (2001), Strain accumulation and rotation in the eastern California shear zone, *J. Geophys. Res.*, 106, 21,995–22,007.
- Scholz, C. (1990), *The Mechanics of Earthquakes and Faulting*, 439 pp., Cambridge Univ. Press, New York.
- Schouten, H., K. D. Klitgord, and D. G. Gallo (1993), Edge-driven microplate kinematics, *J. Geophys. Res.*, 98, 6689–6701.
- Sella, G. F., T. H. Dixon, and A. Mao (2002), REVEL: A model for Recent plate velocities from space geodesy, *J. Geophys. Res.*, 107(B4), 2081, doi:10.1029/2000JB000033.
- Steblov, G. M., M. G. Kogan, R. W. King, C. H. Scholz, R. Bürgmann, and D. I. Frolov (2003), Imprint of the North American plate in Siberia revealed by GPS, *Geophys. Res. Lett.*, 30(18), 1924, doi:10.1029/2003GL017805.
- Tapponnier, P., Z. Xu, F. Roger, B. Meyer, N. Arnaud, G. Wittlinger, and J. Yang (2001), Oblique stepwise rise and growth of the Tibet Plateau, *Science*, 294, 1671–1677.
- Thatcher, W. (1995), Microplate versus continuum descriptions of active tectonic deformation, *J. Geophys. Res.*, 100, 3885–3894.
- Thatcher, W. (2003), GPS constraints on the kinematics of continental deformation, *Int. Geol. Rev.*, 45, 191–212.
- Thatcher, W., G. R. Foulger, B. R. Julian, J. Svart, E. Quilty, and G. W. Bawden (1999), Present-day deformation across the Basin and Range province, western United States, *Science*, 283, 1714–1718.
- Turcotte, D., and G. Schubert (1982), *Geodynamics*, 450 pp., John Wiley, Hoboken, N. J.
- Unruh, J., J. Humphrey, and A. Barron (2003), Transtensional model for the Sierra Nevada frontal fault system, eastern California, *Geology*, 31, 327–330.
- Vollrick, J., R. McCaffrey, G. Sella, C. Stevens, C. Williams, C. McCaffrey, and B. Walton (2003), Block interactions in southern Oregon, northern California, and northwestern Nevada, *Eos Trans. AGU*, 84, Fall Meet. Suppl., Abstract G31B-0712.
- Wallace, L. M., C. W. Stevens, E. Silver, R. McCaffrey, W. Loratung, S. Hasiata, R. Curley, R. Rosa, J. Taugaloidi, and H. Davies (2004a), GPS constraints on active tectonics and arc-continent collision in Papua New Guinea: Evidence for edge-driven microplate rotations, *J. Geophys. Res.*, 109, B05404, doi:10.1029/2003JB002481.
- Wallace, L. M., J. Beavan, R. McCaffrey, and D. Darby (2004b), Subduction zone coupling and tectonic block rotations in the North Island, New Zealand, *J. Geophys. Res.*, 109, B12406, doi:10.1029/2004JB003241.
- Wallace, L., R. McCaffrey, J. Beavan, and S. Ellis (2004c), Association between collision, microplate rotation, and back-arc rifting at obliquely convergent margins in the western Pacific: New insights from geodetic data, *Eos Trans. AGU*, 85, Fall Meet. Suppl., Abstract T41C-1214.
- Wang, K., and T. Dixon (2004), Coupling semantics and science in earthquake research, *Eos Trans. AGU*, 85, 180.
- Wdowinski, S., Y. Sudman, and Y. Bock (2001), Geodetic detection of active faults in S. California, *Geophys. Res. Lett.*, 28, 2321–2324.
- Wesnousky, S. G. (1986), Earthquakes, Quaternary faults, and seismic hazard in California, *J. Geophys. Res.*, 91, 12,587–12,631.
- Wessel, P., and W. H. F. Smith (1998), New, improved version of the Generic Mapping Tools released, *Eos Trans. AGU*, 79, 579.
- Working Group on California Earthquake Probabilities (1995), Seismic hazard in southern California: Probable earthquakes, 1994 to 2024, *Bull. Seismol. Soc. Am.*, 85, 379–439.
- Working Group on Northern California Earthquake Potential (1996), Database of potential sources for earthquakes larger than magnitude 6 in northern California, *U.S. Geol. Surv. Open File Rep.*, 96-705.